The Cerebellum
https://doi.org/10.1007/s12311-021-01303-1

ORIGINAL ARTICLE

Characterisation of the Mouse Cerebellar Proteome in the GFAP-IL6 Model of Chronic Neuroinflammation

Rustam Asgarov[1] · Monokesh K. Sen[2] · Meena Mikhael[3] · Tim Karl[4,5,6] · Erika Gyengesi[1] · David A. Mahns[7] · Chandra S. Malladi[2] · Gerald W. Münch[8]

Accepted: 25 June 2021

Abstract

GFAP-IL6 transgenic mice are characterised by astroglial and microglial activation predominantly in the cerebellum, hallmarks of many neuroinflammatory conditions. However, information available regarding the proteome profile associated with IL-6 overexpression in the mouse brain is limited. This study investigated the cerebellum proteome using a top-down proteomics approach using 2-dimensional gel electrophoresis followed by liquid chromatography-coupled tandem mass spectrometry and correlated these data with motor deficits using the elevated beam walking and accelerod tests. In a detailed proteomic analysis, a total of 67 differentially expressed proteoforms including 47 cytosolic and 20 membrane-bound proteoforms were identified. Bioinformatics and literature mining analyses revealed that these proteins were associated with three distinct classes: metabolic and neurodegenerative processes as well as protein aggregation. The GFAP-IL6 mice exhibited impaired motor skills in the elevated beam walking test measured by their average scores of 'number of footslips' and 'time to traverse' values. Correlation of the proteoforms' expression levels with the motor test scores showed a significant positive correlation to peroxiredoxin-6 and negative correlation to alpha-internexin and mitochondrial cristae subunit Mic19. These findings suggest that the observed changes in the proteoform levels caused by IL-6 overexpression might contribute to the motor function deficits.

Keywords Chronic inflammation · Motor function · Top-down proteomics · Bioinformatics · Neurodegeneration · Metabolic dysregulation · Protein aggregation

Introduction

Clinical and preclinical evidence suggests chronic inflammation as a significant pathogenic process driving the progression of neurodegenerative conditions such as Alzheimer's disease (AD), the pathoetiology of which remains unclear [1–4]. The neuroinflammatory process is characterised by excessive release of various cytotoxic cytokines including interleukin-6 (IL-6) leading to reactive gliosis (i.e. reactivity of microglia and astroglia) [5, 6]. IL-6 is a potent proinflammatory mediator and its role is particularly important as its expression increases in normal ageing and neurological disease [7, 8]. Studies have also shown increased levels of IL-6 in the post-mortem brains of AD patients [9]. Elevated levels of systemic IL-6 have been correlated with lower white matter integrity in the brain and cognitive decline in older individuals in an age-dependent manner using neuroimaging and cognitive tests [10, 11].

It was reported that IL-6 could also induce neuronal protein tau hyperphosphorylation, altered electrophysiological

✉ Gerald W. Münch
G.Muench@westernsydney.edu.au

1 Pharmacology Unit, School of Medicine, Western Sydney University, Penrith, NSW, Australia

2 Proteomics and Lipidomics Lab, School of Medicine, Western Sydney University, Penrith, NSW, Australia

3 Mass Spectrometry Facility, School of Medicine, Western Sydney University, Penrith, NSW, Australia

4 Behavioural Neuroscience Lab, School of Medicine, Western Sydney University, Penrith, NSW, Australia

5 Neuroscience Research Australia (NeuRA), Randwick, NSW 2031, Australia

6 School of Medical Sciences, University of New South Wales, Kensington, NSW, Australia

7 Integrative Physiology Lab, School of Medicine, Western Sydney University, Penrith, NSW, Australia

8 School of Medicine, Western Sydney University, Locked Bag 1797, Penrith, NSW 2751, Australia

Published online: 29 July 2021

activity and calcium signalling in cerebellar Purkinje cells [12, 13]. Therefore, an animal model with a chronic expression of IL-6 in the brain could provide a better understanding of functional and structural changes as a result of the inflammatory cascade initiated by IL-6 [14]. The transgenic GFAP-IL6 mouse is a model of chronic neuroinflammation with astrocyte-targeted overexpression of IL-6 in the brain [14]. GFAP-IL6 mice exhibit neurological-like disease with inflammatory processes and degeneration in the brain. Homozygous GFAP-IL6 mice express 8 copies of the transgene while heterozygous mice express 4 copies [14]. The inflammatory response in the brains of GFAP-IL6 mice involves elevated levels of IL-6, tumour necrosis factor-α, IL-1, intercellular adhesion molecule-1, activation of microglia and astrocytes [1, 14–16]. The resultant neurodegenerative changes include the breakdown of the blood–brain barrier, pathological deposition of oxidated products, iron, dystrophy and loss of Purkinje neuron dendritic processes in the cerebellum region of homozygous mice [14, 17]. The cerebellar atrophy and loss of synapses and neurons in the brain lead to motor and memory function deficits of the GFAP-IL6 mice [1, 14, 16, 18].

Proteome analysis is a powerful tool to investigate changes in protein profiles for disease state (i.e. protein up or downregulation, biomarker discovery), their association with other protein networks and to understand the role of different proteoforms in a normal physiological state as well as various pathophysiological conditions [19–21]. The effects of the IL-6-initiated inflammatory cascade can be understood by assessment of cerebellum-based motor function and correlation with cerebellum proteome analysis of GFAP-IL6 mice which may lead to the discovery of new targets for effective treatment of neuroinflammatory neurodegenerative diseases [22, 23]. The function and abundance of proteoforms in biological systems may be altered via post-translational processes without involving transcriptional mechanisms [19, 24, 25]. Concerning this, the discovery of proteome alterations has enabled a better understanding of consequential and adaptive mechanisms in neurodegenerative diseases [25, 26].

Top-down proteomic analysis is a common approach in biomedical research that employs 2-dimensional gel electrophoresis (2-DE) of protein samples followed by mass spectrometry analysis of protein spots of interest [25, 27–29]. It provides a great advantage by allowing robust assay to resolve protein species and their isoforms based on their isoelectric points (pI) and molecular weights (MW) [30–32]. The separated proteins are stained, and gel images are quantitatively analysed to identify protein spots with significant changes [25, 33–35]. The protein of each selected spot can be identified using peptide mass fingerprint data generated by the liquid chromatography-tandem mass spectrometry (LC–MS/MS) and queries in the bioinformatics database [25, 36, 37]. In this study, we assessed motor functions at 9 months of age and subsequently analysed the cerebellar proteome of heterozygous GFAP-IL6 mice in comparison to wild type (WT) C57BL/6J mice to identify significant changes in protein profiles (upregulated or downregulated) associated with the motor deficits of the transgenic mice. We found a marked alteration in cerebellar proteoforms and deficits in motor function of the GFAP-IL6 mice. Most importantly, a subset of the proteoforms was correlated with the motor scores indicating cerebellum proteome changes are associated with behavioural deficits of the GFAP-IL6 mice.

Materials and Methods

Ethics Statement and Experimental Animals

All animal research procedures were performed according to the Western Sydney University Animal Care and Ethics Committee (ACEC) guidelines and approvals (Animal Research Authority code: A10057) and followed the Australian Code of Practice for the Care and Use of Animals for Scientific Purposes. The general health condition and body weights of the mice were monitored and recorded in 2 weeks' intervals in line with the ACEC guidelines. The body weight data was statistically analysed as part of their general health assessment. The study was conducted by selecting 9-month-old male heterozygous GFAP-IL6 mice (n = 8) and wild type-like (WT) control (C57BL/6J, n = 9) littermates by group-housing them in individually ventilated cages (GM500 Mouse IVC, Techniplast, UK) in the animal facility. The decision on the age of the mice was based on the histological (i.e. marked gliosis and neurodegeneration) and motor function changes previously published by our group [1, 16]. Mouse food pellets were obtained from Specialty Feeds (Glen Forrest, WA, Australia) following the National Health and Medical Research Council guidelines for mice and were fed to the mice with water ad libitum. The animal facility was operated with a 12:12-h light–dark cycle with control of temperature (22–23℃) and humidity (40–60%).

Behavioural Tests

Male GFAP-IL6 (n = 8) mice and WT (n = 9) littermates were handled by the same experimenter for three consecutive days involving 2 min of handling per mouse each day. On test days, the mice were transported to the experimental laboratory and left undisturbed for 30 min for adaptation. Handling and transport of the mice for behavioural testing were conducted according to the laboratory protocol based on previous publications [38, 39].

Elevated Beam Walking Test

Motor learning and performance of the mice were measured by the elevated beam walking test which allows sensitive assessment of motor skills such as coordination, balance and muscle function [1, 40, 41] and well-established standard protocols were used [42, 43]. The custom-made test apparatus consisted of an elevated narrow beam with 52-cm height, 1-m length, 0.4-cm width upper surface and 1.5-cm width lower surface. Aversive 800 lx bright light from 60-W lamp was positioned close to the starting point on the beam (Supplementary Fig. 1A). The test procedure involved training the mice to walk on the beam for two consecutive days and testing their motor learning and performance on the 3rd day. The training of the mice was assisted by the experimenter on the 1st day of the test to encourage them to walk towards the safety of their home cages located at the end of the beam. Each mouse was given three trials per day with an inter-trial interval of at least 30 s to 1 min during both training and testing days. The apparatus was thoroughly cleaned with 70% ethanol and completely dried with absorbent paper towels between each trial. Test performance was quantified by measurement of 'number of footslips' and 'time to traverse' values of each mouse on the testing day. The footslips' measurement accounted for errors made by only the hind limbs of each animal. Motor performance of the experimental groups was compared by statistical analysis of the average 'number of footslips' and 'time to traverse' scores of the mice across the trials.

Accelerod Test

The accelerod test allows assessing motor function and learning performance of mice by quantitative measurement of their coordination and balance skills on an accelerating rotarod [1, 16, 40, 41]. A commercially available test apparatus (Model 47600, Ugo Basile, Italy) was used which consists of a rod in 3-cm diameter and 30-cm height and rotating around its axis (Supplementary Fig. 1B). The accelerod was designed with a knurled surface to provide support for paw gripping of mice while they try to maintain balance on the accelerod. The apparatus allowed testing up to five animals simultaneously by providing individual partition of equal width. Each compartment was confined by large diameter plastic barriers on both sides to prevent animal escape and distraction from other mice. The accelerod skills of the mice were assessed 48 h after the elevated beam walking test. Each mouse was given three testing trials with an inter-trial interval of 30–40 min for resting. The apparatus was thoroughly cleaned with 70% ethanol and completely dried with absorbent paper towels between each trial. The protocol involved an assessment of the motor performance of the mice on an accelerating rotarod for a maximum time of 300 s. The accelerod was started with constant 4 rpm speed and uniformly accelerated to 40 rpm speed. The acceleration of the speed was approximately 7.2 rpm increase per minute meaning that speed reached 40 rpm at 300 s. The accelerod performance of the experimental groups was compared by statistical analysis of averaged and best 'time to fall' scores of the mice across all three trials.

Sample Collection and Tissue Homogenisation

After completion of the motor tests, the mice were euthanised using an overdose of anaesthetic pentobarbitone (250 mg/kg, Lethobarb^{TM}, Tory laboratories, Glendenning, NSW, Australia) exposure. Three male mice from each group were randomly selected for proteomic analysis. The brains were dissected, quickly washed in cold (4℃) 0.01 M phosphate-buffered saline (PBS) containing 0.004 mg/mL concentration of cocktail (MSSAFE-5VL, Sigma-Aldrich, St. Louis, MO, USA) of protease inhibitors (bestatin hydrochloride, leupeptin, phosphoramidon disodium salt, pepstatin A, elastatinal, aprotinin, nafamostat mesylate, antipain) and phosphatase inhibitors (okadaic acid, sodium fluoride, sodium orthovanadate, bromotetramisole oxalate) to wash the blood and prevent any proteolysis. The cerebellum was dissected using a sharp scalpel and immediately snap-frozen in liquid nitrogen (− 196℃) and stored at − 80℃ until further use. The cerebellum tissue was pulverised by applying an automated frozen disruption procedure [27] and using Mikro-Dismembrator (Sartorius, Göttingen, LS, Germany). Polytetrafluoroethylene (Teflon) chambers along with a grinding ball made of chromium steel were pre-cooled in liquid nitrogen for 5 min. Frozen whole cerebellum was placed into the cold Teflon chamber and homogenised at 2000 rpm for 30 s and powder was stored at − 80℃ until further use [25].

Protein Fractionation

Total soluble and membrane protein fractionation was performed by resuspending 0.97 ± 0.16 g of each pulverised cerebellum tissue in three times the volume of hypotonic lysis buffer (20 mM HEPES, pH 7.4 containing EDTA-free protease and phosphatase inhibitors). An equal volume of 0.02 M PBS was added to the sample mixture and was kept on ice for 1 min. Then the sample was centrifuged at 109×10^3 g force for 3 h at 4℃ using SW 55 Ti rotor in Beckman Coulter Optima L-100 XP ultracentrifuge (Beckman Coulter, Indianapolis, IN, USA). After the centrifugation, the supernatant was collected as a total cytosolic/soluble protein (SP) fraction and retained the pellet as a membrane protein (MP) fraction. PBS buffer from SP was exchanged with 4 M urea buffer using a 3-kD cut-off filter tube (Amicon, Ultra-4 centrifugal filter devices, Merck-Millipore, Burlington, MA, USA) to 500 µL and stored at − 80℃. The

pellet was collected as total MP fraction and solubilised in 500 µL of solubilisation buffer containing 8 M urea, 2 M thiourea, 4% CHAPS with protease and phosphatase inhibitors, centrifuged at 109×10^3 g force at 4℃ for 1 h, aliquoted, the supernatant was snap-frozen and stored at − 80℃ [25, 44]. The protein was quantified by using EZQ fluorescent dye (Invitrogen, Carlsbad, CA, USA) and bovine serum albumin (BSA, Amresco, Solon, OH, USA) as standard as shown before [45, 46].

Sample Treatment: Disulphide Reduction and Alkylation

Each protein sample with a concentration of 100 µg was prepared by adding solubilisation buffer, a mixture of carrier ampholytes, reducing agent tributylphosphine (TBP) and acrylamide solution to a final volume of 125 µL during rehydration with 3–10 broad pH range non-linear immobilised pH gradient (IPG) strip (Bio-Rad, Hercules, CA, USA). Initially, each sample was mixed with a buffer containing 8 M urea, 2 M thiourea, 4% CHAPS containing protease-phosphatase inhibitors followed by 2% ampholytes before subjected to disulphide reduction. The reduction of proteins in the sample was performed by adding a reducing buffer containing 45 mM 1,4-dithiothreitol (Merck, Darmstadt, HE, Germany) and 2.3 mM tributylphosphine (Bio-Rad, Hercules, CA, USA), respectively. Immediately, all the above-treated samples were incubated at 25℃ for 60 min. The alkylation step was carried out after incubation by adding freshly prepared acrylamide solution (final concentration 230 mM) and incubated for a further 60 min at 25℃. All treated samples containing 100 µg proteins were loaded to 7 cm IPG strips and rehydrated for 16 h at room temperature [25, 47, 48].

Protein Separation by 2-DE Method

Initially, proteins were separated by the net charge of protein (i.e. isoelectric point, pI; first dimension) and subsequently based on protein molecular weight (second dimension). During the first dimension, rehydrated IPG strips were transferred to the focusing tray and overlayed with mineral oil (Bio-Rad) to prevent sample evaporation during the focussing step. Electrical contact was established by placing one wet filter paper wick (2.5 cm × 4 mm) between both positive and negative ends of the platinum electrodes and IEF gel. The loaded tray was then transferred to the Protean IEF Cell (Bio-Rad) machine for the run. The isoelectric focusing was performed at 4000 V, current 50 µA/strip was applied for 37,500 V hours at 17℃. Once focusing was completed, mineral oil was drained from the strips, placed into a clean rehydration tray and immediately subjected to the second dimension on 12.5% SDS-PAGE. Before subjected to the second dimension, focussed proteins were reduced and alkylated by adding 2 mL of equilibration buffer to each IPG strip (6 M urea, 20% glycerol, 2% SDS, 375 mM Tris (pH 8.8) and 130 mM DTT) for 10 min at room temperature. Immediately after reduction step, all strips were transferred to 2 mL of 350 mM acrylamide solution (6 M urea, 20% glycerol, 2% SDS, 375 mM Tris (pH 8.8)) for alkylation and incubated for further 10 min. After alkylation, second dimension (SDS-PAGE) was carried along with molecular weight markers. The gels were quickly transferred to a cold room (4℃) and placed into a Mini-Protean (Bio-Rad) electrophoretic tank with a running buffer (0.3% Tris, 1.44% glycine, 0.1% SDS). Electrophoresis was carried out at 90 V until tracking dye bromophenol blue reached the bottom of the gel [25, 47, 48].

Gel Staining, Imaging and Protein Spot Analysis

After completion of the electrophoresis, the gels were fixed with a solution containing 10% methanol and 7% acetic acid for 1 h on an orbital shaker (50 rpm/min). Then the gels were washed with distilled water for 3 × 30 min and stained with freshly prepared 50 mL of Colloidal Coomassie Brilliant Blue (G-250, Merck) solution and left on a shaker for 20 h at room temperature. After staining, the gels were destained with a 0.5% NaCl solution for 5 × 15 min [25, 47, 48] and imaged using ImageQuant™ FUJI LAS-4000 biomolecular imager (GE Healthcare, Chicago, IL, USA). The image analysis was carried out using Delta2D software [DECODON, Greifswald, Germany]; [25, 48]. Protein spot analysis from the imaged gels was carried out as per the manufacturer's manual. In a nutshell, automatic warping mode was selected for warping both within the groups (n = 3) and between the groups (n = 3), and spots were sorted for their 'percent normalised spot volume' values, 'average grey' values, 'mean normalised volume' and 'Student's t-test p-values' for the transgenic versus control groups. All significant protein spots with a p-value of less than 0.05 were selected for protein identification using liquid chromatography-tandem mass spectrometry [LC–MS/MS]; [25, 48].

In-gel Digestion and Peptide Extraction

The protein spots from both SP and MP gels were excised and equilibrated with 400 µL of 50 mM ammonium bicarbonate buffer and destained with 2 × 200 µL 50 mM ammonium bicarbonate containing 50% acetonitrile for 10 min. The destained gel pieces were then dehydrated for 5 min by adding 200 µL of 100% acetonitrile. After removing the acetonitrile, the gel pieces were completely dried and digested by adding freshly prepared trypsin (Trypsin Gold, Mass Spectrometry Grade, Promega Corp, V5280) solution with a concentration of 12.5 ng/µL and incubated at 4℃ overnight. The next day, the peptide solution was collected after 30-min bath sonication and transferred to a fresh tube.

The final peptide sample volume was reduced to 14 µL using SpeedVac™ vacuum concentrator (1400 rpm for 10 min). Finally, the samples were transferred to glass vials for subsequent LC–MS/MS analysis as described before [25, 47, 48].

Liquid Chromatography-Tandem Mass Spectrometry Analysis

The extracted peptide sample vials were placed in a sample plate of nanoAcquity UPLC (Waters, Milford, MA, USA) attached to a SynaptG2-Si HDMS (Waters) mass spectrometer which is a combination of ultra-performance liquid chromatography and ESI tandem mass spectrometry (UPLC-MS/MS). Three microliters of each sample were injected into M/Z Symmetry C18 trapping column (180 µm × 20 mm) and washed at a flow rate of 5 µL/min and passed through BEH130 C18 (Waters) analytical column (75 µm × 100 mm) packed with 130 $A^0 \times 1.7$ µm particles for UPLC run. Peptides bound to the C18 column were eluted at 0.3 µL/min flow rate of mobile phase solvents A (water) and B (acetonitrile). Gradient elution of the peptides was initially performed at 1% B then gradually raised to 40% B in 40 min and 85% B in the next 2 min for the MS/MS analysis. The MS analysis of each sample was completed in a total of 50 min. After completion of the mass spectrometry, raw mass spectra data were analysed in the Protein Lynx Global Server (PLGS). Data were analysed using the following setup: species-*Mus musculus*, databank-UniProt (https://www.uniprot.org/), lock mass window-0.25 Da, low energy threshold-500, enzyme-trypsin, missed cleavages-2, fixed modifier reagents: carbamidomethyl C, variable modifier reagent: deamidation N, deamidation Q, oxidation M and false discovery rate-4. The identified proteins were selected by the following criteria: (1) the highest PLGS score (> 80) with a sequence coverage ≥ 15%; and (2) ≥ 3 unique matched peptides [25, 47, 48]. The top scorer from the list is provided in Table 1, and the rest of the proteins corresponding to each spot have been provided in the Supplementary Excel file. The experimental MW and pI of the protein spots were calculated by linear fit curve formula obtained from X, Y plotting of refractive index MW versus Log MW, refractive index pI versus Log pI of the molecular weight and pI standards, respectively [25]. The experimental MW and pI are presented in Table 1.

Literature Mining and Bioinformatics

The identified proteins were reviewed in the literature using PubMed (www.ncbi.nlm.nih.gov/pubmed). Functional annotation and network of the proteins were analysed by a query in DAVID V6.8 (Database for Annotation, Visualization and Integrated Discovery, https://david.ncifcrf.gov/home.jsp) and STRING V11.0 (Search Tool for the Retrieval of Interacting Genes/Proteins, https://string-db.org/) websites using the list of their UniProt accession numbers [25].

Statistical Analysis

Data obtained by body weight measurement, elevated beam walking and accelerod tests were statistically analysed using the SPSS software (IBM Corp, USA). Body weight data was analysed using the general linear model and applying repeated measures analysis of variance (RM ANOVA). If a significant p-value was displayed by Mauchly's test in the RM ANOVA, then data analysis was performed by the mixed models linear and applying autoregressive or heterogeneous autoregressive covariance matrix model. The motor performance of the experimental groups was compared by univariate ANOVA of the averaged scores of the mice in the elevated beam walking and averaged and best scores in the accelerod test. The average motor score of each mouse was calculated by the average value of its two trials with the best performances in each motor test measure. The reason for the selection of two trials with the best values is to minimise the effect of possible confounding behaviour of the mice during the trials on their motor scores. Genotype was defined as between the subjects' factors. Pearson test (two-tailed) was used for bivariate correlation of the averaged and best scores of motor function of each mouse to the normalised spot volume of each protein from its cerebellum. GraphPad Prism 8 (www.graphpad.com, San Diego, CA, USA) was used for post hoc multiple comparison analysis of the body weights by applying Sidak's test and graphical presentation of all data. Statistically significant results are shown by $*p < 0.05$, $**p < 0.01$ and $***p < 0.001$ values in the figures. Image processing software CorelDRAW (V2019; www.coreldraw.com, Canada) was used for figure assembly.

Results

Body Weight Analysis

We conducted a comparative statistical analysis of the body weights of the heterozygous GFAP-IL6 and WT mice over 6 months to examine whether IL-6 overexpression caused adverse effects on general health. Both groups exhibited significantly increased body weights over time [$F(13, 233.797) = 66.141$, $p < 0.001$]. Although GFAP-IL6 mice exhibited a trend of lower body weights after the 10th week of monitoring, this effect of the genotype was not statistically significant [$F(1, 37.390) = 2.621$, $p = 0.114$] as we observed previously [1]. Furthermore, the difference in body weights of the groups was not statistically significant at all time points of measurement assessed by multiple comparisons test (Fig. 1A).

Table 1 2DE LC–MS/MS analysis identified a total of 67 proteins from the WT and GFAP-IL6 groups

Spot ID	UniProt Accession ID	Gene ID	Protein name	PLGS score	Theoretical MW (kD)/pI	Experimental MW (kD)/pI	Unique peptides	Sequence coverage (%)	Protein fold change	Unique peptides
S1	P16125	Ldhb	L-lactate dehydrogenase B chain	4510	37/5.6	56/5.2	61	44	0.54	(K)LIASVADDEAAVPNNK(I) (K)IVADKDYSVTANSK(I)
S2	O08709	Prdx6	Peroxiredoxin-6	4620	25/5.6	33/5.3	86	71	1.51	(K)KGESVMVVPTLSEEEAK(Q) (K)LKLSILYPATTGR(N)
S3	P28651	Cah8	Carbonic anhydrase-related protein	6818	33/4.5	52/4.5	46	41	0.59	(K)AVTEILQDIQYK(G) (R)YPLTISQMQIEEFR(R)
S4	P70296	Pebp1	Phosphatidylethanolamine-binding protein 1	3256	21/5.0	28/4.7	9	51	0.68	(K)LYTLVLTDPDAPSR(K) (R)VDYAGVTVDELGK(V)
S5	P63242	If5a1	Eukaryotic translation initiation factor 5A-1	1763	17/4.9	17/4.7	26	36	0.67	(R)EDLRLPEGDLGKEIEQK(Y) (K)VHLVGIDIFTGK(K)
S6	P15105	Glna	Glutamine synthetase	10,460	42/6.7	64/6.2	85	39	0.81	(K)AYGRDIVEAHYR(A) (K)YNRKPAETNLR(H)
S7	P17751	Tpis	Triosephosphate isomerase	6112	32/5.4	32/6.3	101	62	1.14	(K)VTNGAFTGEISPGMIK(D) (R)RHVFGESDELIGQK(V)
S8	P00920	Cah2	Carbonic anhydrase 2	2271	29/6.5	37/5.9	29	50	1.26	(R)EPITVSSEQMSHFR(T) (K)DFPIANGDR(Q)
S9	Q9EQU5	Set	Protein SET	2249	33/4.0	58/4.2	49	26	0.61	(K)EFHLNESGDPSSK(S) (R)LNEQASEEILKVEQK(Y)
S10	P16125	Ldhb	L-lactate dehydrogenase B chain	4186	37/5.6	56/5.1	33	48	0.54	(K)IVADKDYSVTANSK(I) (K)LIASVADDEAAVPNNK(I)
S11	Q9R0P3	Estd	S-formylglutathione hydrolase	4476	31/6.8	44/6.3	36	44	0.64	(K)VFEHSSVELK(C) (K)KAFSGYLGPDESK(W)
S12	Q9R0P9	Uchl1	Ubiquitin carboxyl-terminal hydrolase isozyme L1	4508	25/5.0	33/4.8	103	69	0.77	NEAIQAAHDSVAQEGQCR KQIEELKGQEVSPK
S13	O08553	Dpyl2	Dihydropyrimidinase-related protein 2	4514	62/5.9	95/5.2	42	50	1.36	(K)QIGENLIVPGGVK(T) (K)MDENQFVAVTSTNAAK(V)
S14	P17751	Tpis	Triosephosphate isomerase	4710	32/5.4	32/5.8	51	53	1.13	(R)HVFGESDELIGQK(V) (K)VTNGAFTGEISPGMIK(D)
S15	P12658	Calb1	Calbindin	6998	30/4.5	33/4.4	111	76	0.70	(K)NKQELDINNITTYKK(N) (R)KYDTDHSGFIETEELK(N)
S16	Q9JJV2	Prof2	Profilin-2	1040	15/6.8	13/5.8	6	26	0.88	(K)SQGGEPTYNVAVGR(A) (R)EGFFTNGLTLGAK(K)
S17	P15532	Ndka	Nucleoside diphosphate kinase A	6360	17/7.3	15/6.1	19	74	0.82	(R)TFIAIKPDGVQR(G) (K)FLQASEDLLK(E)
S18	P01942	Hba	Hemoglobin subunit alpha	5798	15/8.6	11/6.9	28	75	1.29	(K)IGGHGAEYGAEALER(M) (K)FLASVSTVLTSK(Y)
S19	O08553	Dpyl2	Dihydropyrimidinase-related protein 2	19,218	62/5.9	95/5.4	68	61	1.43	IVLEDGTLHVTEGSGR SAAEVIAQAR
S20	P35700	Prdx1	Peroxiredoxin-1	4388	22/8.2	27/6.2	35	53	0.78	QITINDLPVGR LVQAFQFTDK

Table 1 (continued)

Spot ID	UniProt Accession ID	Gene ID	Protein name	PLGS score	Theoretical MW (kD)/pI	Experimental MW (kD)/pI	Unique peptides	Sequence coverage (%)	Protein fold change	Unique peptides
S21	Q9CWZ7	Snag	Gamma-soluble NSF attachment protein	4099	35/5.1	56/5.0	27	47	0.79	LGLSLVVPGGGIK FDEAALSIQKEK
S22	P05064	Aldoa	Fructose-bisphosphate aldolase A	5794	39/8.1	60/6.8	57	46	1.24	LQSIGTENTEENRR ADDGRPFPQVIK
S23	Q3UYG1	Cc160	Coiled-coil domain-containing protein 160	85	37/9.8	88/5.9	12	35	0.74	AVNFQEPGTGASKK LHLLNEELGELSLK
S24	P16125	Ldhb	L-lactate dehydrogenase B chain	5966	37/5.6	51/5.4	66	50	0.79	IVADKDYSVTANSK LKDDEVAQLR
S25	P99029	Prdx5	Peroxiredoxin-5	3650	22/9.1	15/6.9	25	32	0.79	VGDAIPSVEVFEGEPGKK THLPGFVEQAGALK
S26	Q9JJV2	Prof2	Profilin-2	3657	15/6.8	13/5.4	31	41	0.70	DREGFFTNGLTLGAK SQGGEPTYNVAVGR
S27	P05213	Tba1b	Tubulin alpha-1B chain	7160	50/4.8	81/5.7	9	21	0.72	VGINYQPPTVVPGGDLAK NLDIERPTYTNLNR
S28	O08709	Prdx6	Peroxiredoxin-6	3515	25/5.6	33/5.4	56	62	1.34	DINAYNGETPTEK PGGLLLGDEAPNFEANTTIGR
S29	Q60631	Grb2	Growth factor receptor-bound protein 2	3804	25/5.9	31/5.4	30	44	0.80	FNSLNELVDYHR ESESAPGDFSLSVK
S30	P63328	Pp2ba	Serine/threonine-protein phosphatase 2B catalytic subunit alpha isoform	1713	59/5.5	43/5.4	25	17	0.60	LFEVGGSPANTR TQEHFTHNTVR
S31	P17742	Ppia	Peptidyl-prolyl cis–trans isomerase A	3724	18/8.0	17/6.3	39	43	0.90	VKEGMNIVEAMER VSFELFADKVPK
S32	P05213	Tba1b	Tubulin alpha-1B chain	10,295	50/4.8	78/5.1	14	31	0.80	NLDIERPTYTNLNR VGINYQPPTVVPGGDLAK
S33	P63017	Hsp7c	Heat shock cognate 71-kD protein	19,182	71/5.2	97/4.8	122	61	1.48	VEIIANDQGNR STAGDTHLGGEDFDNR
S34	Q99LX0	Park7	Protein/nucleic acid deglycase DJ-1	4922	20/6.4	28/5.6	51	61	0.74	GAEEMETVIPVDVMRR AGIKVTVAGLAGK
S35	O08553	Dpyl2	Dihydropyrimidinase-related protein 2	3049	62/5.9	93/5.7	37	33	0.83	DNFTLIPEGTNGTEER QIGENLIVPGGVK
S36	P80314	Tcpb	T-complex protein 1 subunit beta	13,156	57/6.0	77/5.6	80	41	0.76	EALLSSAVDHGSDEAR VAEIEHAEKEK
S37	Q9R1P4	Psa1	Proteasome subunit alpha type 1	5822	30/6.0	40/5.7	40	51	0.68	FVFDRPLPVSR ETLPAEQDLTTK
S38	Q921I1	Trfe	Serotransferrin	1625	77/6.9	105/6.0	22	19	1.72	GTDFQLNQLEGK DGGGDVAFVK

Table 1 (continued)

Spot ID	UniProt Accession ID	Gene ID	Protein name	PLGS score	Theoretical MW (kD)/ pI	Experimental MW (kD)/pI	Unique peptides	Sequence coverage (%)	Protein fold change	Unique peptides
S39	P63101	1433z	14–3-3 protein zeta/delta	13,005	28/4.5	39/4.4	30	45	0.89	GIVDQSQQAYQEAFEISK SVTEQGAELSNEER
S40	Q99LD8	Ddah2	N(G)_N(G)-dimethylarginine dimethylaminohydrolase 2	5305	30/5.6	37/5.2	18	35	0.80	DFAVSTVPVSGSSHLR GGGDLPNSQEALQK
S41	P28663	Snab	Beta-soluble NSF attachment protein	9318	34/5.2	46/4.9	57	74	0.48	VAAYAAQLEQYQK HDSATSFVDAGNAYK
S42	P18760	Cof1	Cofilin-1	1889	19/8.2	19/6.7	11	35	0.83	YALYDATYETK LGGSAVISLEGKPL
S43	P39053	Dyn1	Dynamin-1	4874	98/7.6	113/5.9	110	48	0.77	IEGSGDQIDTYELSGGAR VLNQQLTNHIR
S44	P47738	Aldh2	Aldehyde dehydrogenase	13,977	57/7.5	75/5.8	47	38	0.69	TIPIDGDFFSYTR TEQGPQVDETQFKK
S45	O08553	Dpyl2	Dihydropyrimidinase-related protein 2	20,991	62/5.9	88/5.7	165	64	0.84	AVGKDNFTLIPEGTNGTEER NLHQSGFSLSGAQIDDNIPR
S46	Q9D898	Arp5l	Actin-related protein 2/3 complex subunit 5-like protein	4731	17/6.4	19/5.8	25	43	0.66	SSEIEQAVQSLDR ALAVGGLGSIIR
S47	Q9JL62	Gltp	Glycolipid transfer protein	3729	24/7.2	24/6.3	46	49	0.60	VGATLALLWLK GQNVTEEECLEK
M1	P17182	Enoa	Alpha enolase	6507	47/6.4	95/4.8	57	65	1.43	(R)IGAEVYHNLK(N) (R)YITPDQLADLYK(S)
M2	P08551	Nfl	Neurofilament light polypeptide	6685	61/4.4	89/4.6	205	78	1.34	(K)RIDSLMDEIAFLKK(V) (K)NMQNAEEWFK(S)
M3	P46660	Ainx	Alpha-internexin	21,098	55/5.2	81/5.3	212	68	0.64	(K)VGEGFEETLGEAVISTK(K) (R)TNEKEQLQGLNDR(F)
M4	P16330	Cn37	2'_3'-cyclic-nucleotide 3'-phosphodiesterase	3312	47/9.3	62/6.7	36	31	0.82	(K)AGQVFLEELGNHK(A) (K)NQWQLSADDLKK(L)
M5	P05063	Aldoc	Fructose-bisphosphate aldolase C	7702	39/6.7	55/6.8	198	72	0.81	(K)GILAADESVGSMAK(R) (R)ALQASALNAWR(G)
M6	P18872	Gnao	Guanine nucleotide-binding protein G(o) subunit alpha	17,650	40/5.2	54/5.0	133	45	0.70	(R)AMDTLGVEYGDKER(K) (K)IIHEDGFSGEDVK(Q)
M7	O08709	Prdx6	Peroxiredoxin-6	3815	25/5.6	32/5.9	60	65	1.38	(K)GESVMVVPTLSEEEAK(Q) (K)LKLSILYPATTGR(N)
M8	Q9CRB9	Mic19	MICOS complex subunit Mic19	4104	26/8.5	35/7.7	24	43	0.70	YSSVYGASVSDEDLK VTTEEYQKAAEEVEAK
M9	P02088	Hbb1	Hemoglobin subunit beta 1	6193	16/7.5	10/7.3	13	53	1.34	VITAFNDGLNHLDSLK VNSDEVGGEALGR
M10	P63017	Hsp7c	Heat shock cognate 71-kD protein	4316	71/5.2	91/5.3	43	39	1.40	STAGDTHLGGEDFDNR TVTNAVVTVPAYFNDSQR

Table 1 (continued)

Spot ID	UniProt Accession ID	Gene ID	Protein name	PLGS score	Theoretical MW (kD)/pI	Experimental MW (kD)/pI	Unique peptides	Sequence coverage (%)	Protein fold change	Unique peptides
M11	Q91VD9	Ndus1	NADH-ubiquinone oxidoreductase 75-kD subunit	2326	80/5.4	97/5.0	107	43	0.79	AVEDKNIGPLVK AQQTKVAVTPPGLAR
M12	P26443	Dhe3	Glutamate dehydrogenase 1	2805	61/8.0	73/6.9	92	40	0.70	HGGTIPVVPTAEFQDR RDDGSWEVIEGYR
M13	Q9D6R2	Idh3a	Isocitrate dehydrogenase [NAD] subunit alpha	2517	40/6.3	53/5.2	34	34	0.80	TPIAAGHPSMNLLLR SNVTAVHKANIMR
M14	Q3UCQ1	Foxk2	Forkhead box protein K2	135	68/9.8	91/5.4	5	15	1.37	FAQSAPGSPLSSQPVLITVQR IDPASESKLVEQAFRK
M15	Q61753	Sera	D-3-phosphoglycerate dehydrogenase	2302	57/6.1	79/5.9	23	23	1.33	AGTGVDNVDLEAATR ILQDGGLQVVEK
M16	Q9QUM9	Psa6	Proteasome subunit alpha type 6	2165	27/6.4	33/6.2	12	17	1.19	AINQGGLTSVAVR ATAAGVKQTESTSFLEK
M17	P48678	Lmna	Prelamin-A/C	2565	74/6.5	88/6.5	48	34	0.76	SGAQASSTPLSPTR LQEKEDLQELNDR
M18	Q8K2B3	Sdha	Succinate dehydrogenase [ubiquinone] flavoprotein subunit	3300	73/7.0	91/6.3	82	30	1.24	VDEYDYSKPIQGQQK GEGGILINSQGER
M19	P52480	Kpym	Pyruvate kinase PKM	1836	58/7.2	81/6.9	51	25	0.80	IISKIENHEGVR GSGTAEVELKKGATLK
M20	P23927	Cryab	Alpha-crystallin B chain	5474	20/6.9	22/6.9	19	32	0.54	TIPITREEKPAVAAAPK EEKPAVAAAPK

S soluble protein, *M* membrane protein, *MW* molecular weight, *pI* isoelectric point. Protein identification was carried out in the ProteinLynx Global Server platform using the UniProt mouse database. Spots with more than one protein hit and the highest PLGS score are shown here. UniProt accession and gene IDs were derived from the UniProt database. The PLGS score, unique peptides, sequence coverage and theoretical (MW/pI) were acquired from the ProteinLynx Global Server platform using the UniProt mouse database search. The experimental MW/pI of full-length protein were determined by calibration of the 2DE gels. The localizations of the proteins are shown in Fig. 2

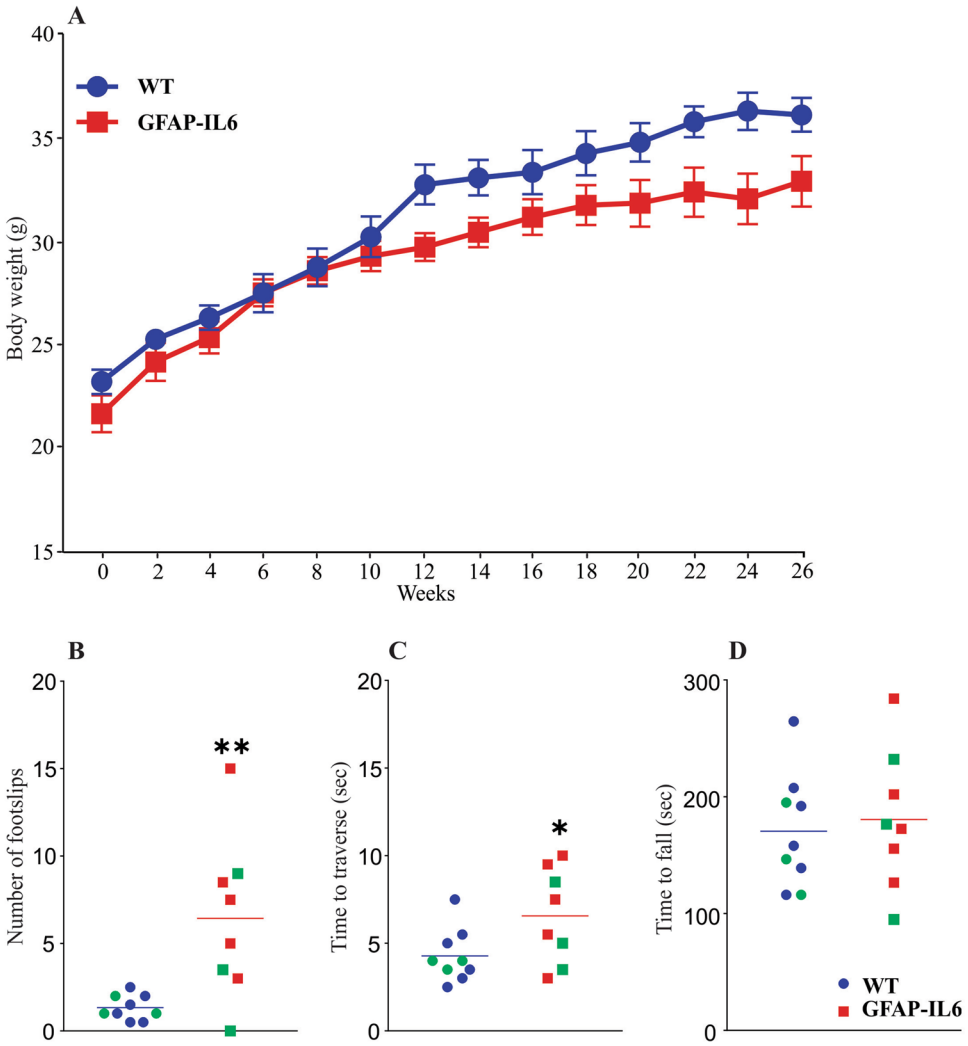

Fig. 1 Body weights and motor test scores of the groups **A** Body weights of both GFAP-IL6 (n = 8) and WT (n = 9) mice increased significantly over time ($p < 0.001$) but had similar body weights across all time points when compared to each other. **B**, **C** GFAP-IL6 mice exhibited significantly higher average scores of 'number of footslips' and 'time to traverse' compared to the WT mice ($p = 0.005$ and $p = 0.045$, respectively). **D** No significant difference was found in average 'time to fall' scores of the groups ($p = 0.708$). Statistically significant results are shown by $*p < 0.05$ and $**p < 0.01$ values in the figures. Mice randomly selected from the GFAP-IL6 (n = 3) and WT (n = 3) groups for cerebellar proteome analysis are depicted in green colour in the motor test graphs

Assessment of Motor Function

The motor function of the mice was assessed by the elevated beam walking and accelerod tasks to examine functional deficits caused by IL-6-induced brain inflammation. Genotype of the mice significantly influenced their average 'number of footslips' [$F(1, 16) = 10.802$, $p = 0.005$] and 'time to traverse' [$F(1, 16) = 4.787$, $p = 0.045$] scores (Fig. 1B, C). The GFAP-IL6 mice had impaired motor performance measured by their higher average scores of 'number of footslips' and 'time to traverse' compared to the WT counterparts. However, average and best 'time to fall' scores of the mice in the accelerod test were not significantly changed by genotype [$F(1, 16) = 0.145$, $p = 0.708$] and [$F(1, 16) = 0.142$, $p = 0.711$], respectively (Fig. 1D). Both groups had similar 'time to fall' scores.

Identification and Quantification of Differentially Regulated Proteoforms

After the behavioural assessment, the whole cerebellar proteome of the mice was assessed using the 2-DE approach coupled with LC–MS/MS to identify changes in proteins' spot abundances. Representative images of the soluble proteome (SP) and membrane proteomes (MP) are shown in Fig. 2A–D. Total spots were counted from soluble and membrane protein gel images of each group. The WT group had a total of 1653 ± 23 spots while the GFAP-IL6 group had 1532 ± 51 spots detected from whole cerebellum SP and MP gel images combined, respectively, as shown in Fig. 2E and 2F. The quantification of SP and MP spots from the WT group showed 828 ± 20 and 825 ± 27 spots and the GFAP-IL6 group showed 788 ± 20 and 744 ± 38 spots, respectively. There was no statistically significant difference between the

groups when their SP spots or MP spots were compared as shown in Fig. 2E. However, the number of total spots was significantly reduced in the GFAP-IL6 group compared to the WT group as shown in Fig. 2F.

Determination of Protein Spot Volumes and Intensities

Delta2D software was used to quantify the normalised spot volumes (i.e. the abundance of resolved proteoforms) and intensities (i.e. average grey values) from the raw gels images (Supplementary Table S1, n = 9 gels/group). The spots with a significant change in normalised volumes between the groups ($P < 0.05$) were excised for protein identification. From the table, in SP, the highest spot volume was found in S18, which presented 2.337 ± 0.154 and 3.009 ± 0.144 values for WT and GFAP-IL6 groups, respectively. In contrast, the lowest spot volume was found in S46, which presented 0.037 ± 0.004 and 0.024 ± 0.003 values for WT and GFAP-IL6 groups, respectively. The highest spot intensity was observed in S18 with values of 0.041 ± 0.0007 and 0.044 ± 0.0020 for WT and GFAP-IL-6 groups, respectively. On the other hand, the lowest spot intensity was observed in S46 with values of 0.003 ± 0.0004 and 0.003 ± 0.0002 for WT and GFAP-IL6 groups, respectively. We also noticed that the SP spots with the highest and lowest normalised spot volumes from both groups presented also the highest and lowest spot intensities. Like SP, the MP spot with the lowest values (M20) followed a similar trend in spot volume and intensity in each group, respectively, but not the MP spot with the highest values. In MP, the highest normalised volume was found in M9 with values of 1.766 ± 0.134 and 2.373 ± 0.169 in WT and GFAP-IL6 groups while the highest spot intensities were present in M18 with values of 0.024 ± 0.0015 and 0.020 ± 0.0011 for the groups, respectively. The SP spots from the GFAP-IL6 mice showed 47 protein spots with significant changes in normalised volume among which 11 protein spots were increased and 36 protein spots were decreased in their spot volumes compared to the WT mice. On the other hand, the MP spots of the GFAP-IL6 mice showed 20 spots with significant changes which included 9 spots with increased spot volume and 11 spots with decreased spot volume compared to the membrane proteome of the WT mice.

Identification of Proteoforms from Soluble and Membrane Fractions After LC–MS/MS

The protein of each spot with a significant volume change was identified by applying selection criteria based on the number of detected unique peptides ($n \geq 3$) and ProteinLynx Global Server (PLGS) score ($n \geq 80$). Table 1 summarises the proteins which have the highest PLGS score, unique peptides and sequence coverage. The proteins with the highest level of PLGS confidence score and a minimum of 3 unique peptides were selected and then protein with the highest PLGS score was identified as the spot protein. The PLGS score for protein hits of each sample is calculated based on statistical algorithms matching peptide mass spectra of the sample from the experimental data with probabilities of all peptide sequences obtained by synthetic digestion of all protein sequences in the search database. All identified proteoforms had a PLGS score exceeding 80, with 3% between 80 and 200, 11% between 1000 and 2000, 14% between 2001 and 3000, 25% between 3001 and 5000, 27% between 5001 and 8000 and 20% exceeding 8000. Moreover, each identification was based at least sequence coverage over 15% with 15–20% for 4 proteins, 21–30% for 6 proteins, 31–40% for 14 proteins, 41–50% for 21 proteins and > 50% for 21 proteins. Likewise, unique peptides were at least 5 unique peptides: only 6% based on 5–10 peptides, but 29% based on 11–30 peptides; 24% based on 31–50 peptides; 17% based on 51–70 peptides; 7% based on 71–100 peptides and even 17% based on over 100 peptides. In addition to the spots with significantly altered volumes, spots uniquely detected by 2-DE only in one of the groups were also excised and analysed which led to the identification of 7 proteins (Supplementary Table S2). Out of 7 proteins, 5 proteins were identified from soluble fraction, whereas 2 proteins from membrane fraction. Interestingly, most of the proteins (6 proteins) were detected from the GFAP-IL6 group, only one protein was found in the WT group (Supplementary Figures S6-S7). All of these identified proteins have a PLGS score over 3290, unique peptides over 15 and sequence coverage over 25 suggesting a high degree of confidence in protein identification.

Bioinformatics Analysis

The identified proteins were queried on the online web tool DAVID Bioinformatics (Database for Annotation, Visualization and Integrated Discovery, NIH, USA) using a functional annotation tool to explore their molecular functions and enriched biological processes [25, 49, 50]. Functional categories defined by DAVID default settings were selected and a minimum of two protein counts and EASE score p-value less than 0.05 were applied for the annotation analysis. The aim was to find out functional and biological process-specific effects of IL-6-induced inflammatory cascade in the cerebellum region. The results of the annotation analysis are shown as bar charts in Fig. 3A and 3B. The interactions of the identified proteins were queried using the online tool STRING (Search Tool for the Retrieval of Interacting Genes/Proteins) by selecting active interaction sources and applying an interaction score of medium confidence (0.4). The analysis showed protein–protein associations which included known

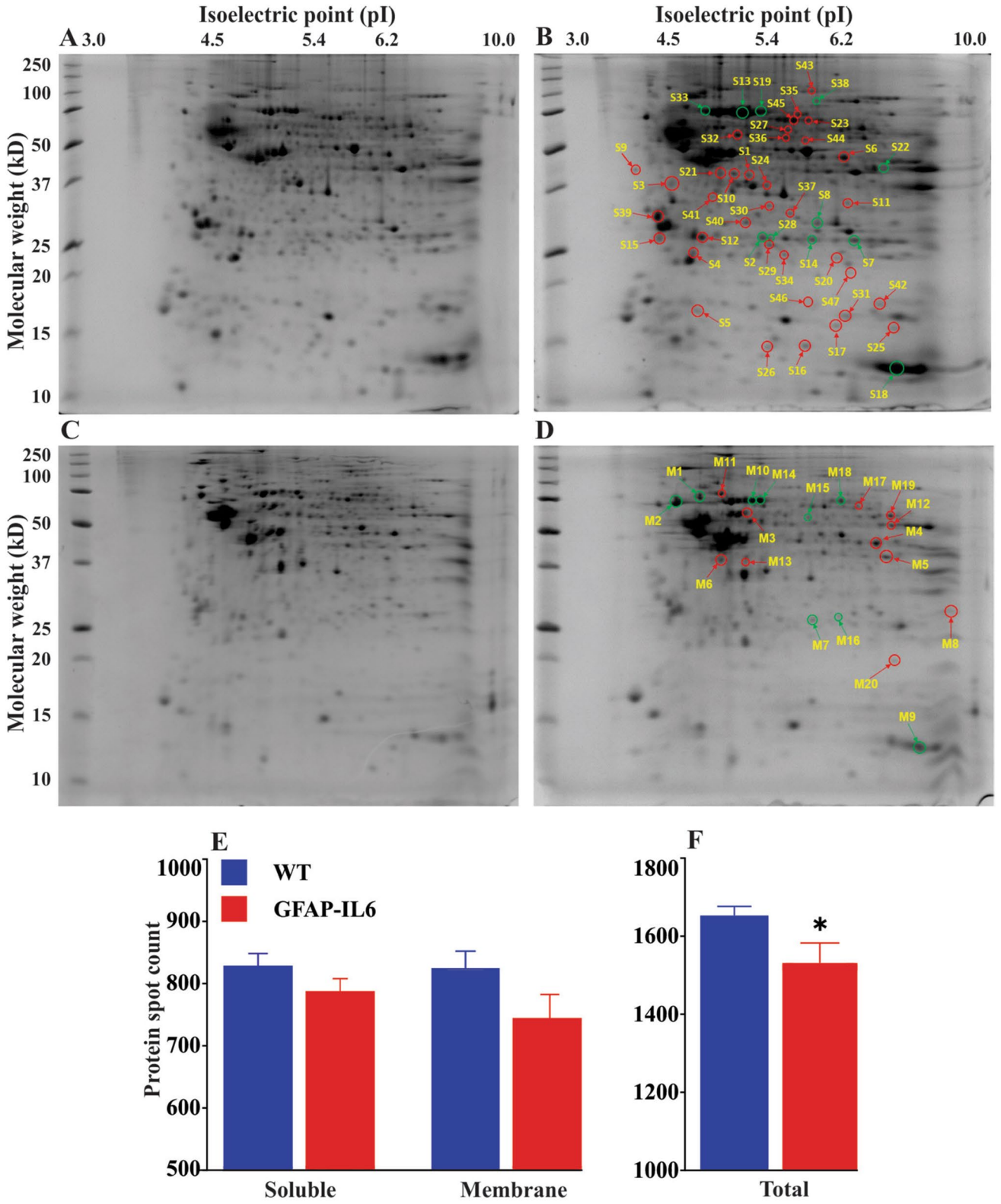

interactions as well as predicted interactions of the proteins as shown in Fig. 3C. The STRING analysis showed direct protein associations of several enzymes of glucose metabolism including triosephosphate isomerase, α-enolase, pyruvate kinase, fructose-bisphosphate aldolase A and C and lactate dehydrogenase which indicates significant regulation of the glycolytic process. In addition, an association of proteoforms involved in oxidative stress response including peroxiredoxin

◂**Fig. 2** The average representative gel images of the total cerebellum soluble and membrane proteome of the WT group **A**, **C** and the GFAP-IL6 group **B**, **D**, respectively. The total number of soluble protein spots detected from WT (828 ± 20) and GFAP-IL6 (788 ± 20) and membrane protein spots from WT (825 ± 27) and GFAP-IL6 (744 ± 39) gel images. **E**, **F** Soluble protein (SP), membrane protein (MP) and total protein (TP) spot counts for the WT and GFAP-IL6 groups are shown by blue and red bars, respectively. **E** Student's t-test did not show a significant difference between WT and GFAP-IL6 groups' soluble protein spot counts ($p = 0.1724$) or membrane protein spot counts ($p = 0.1058$). **F** The GFAP-IL6 group showed significantly lower total protein spot counts compared to the WT group ($p = 0.0455$). Data are presented as mean ± SEM for WT ($n = 9$) and GFAP-IL6 ($n = 9$). Statistically significant differences are shown by $^*p < 0.05$. High magnification separate gel images are provided in the Supplementary Figures S2-7

family members peroxiredoxin-1, peroxiredoxin-5 and peroxiredoxin-6 and protein/nucleic acid deglycase was also revealed by the STRING analysis. Furthermore, this oxidative stress response network was closely linked to the chaperone protein network involved in unfolded protein responses such as heat shock protein 70, T-complex protein 1, and peptidyl-prolyl cis–trans isomerase A and ubiquitin–proteasome networks such as proteasome subunit alpha type-1 and type-6 and ubiquitin carboxyl-terminal hydrolase isozyme L1. It shows the activation of molecular mechanisms to protect against protein misfolding and aggregation as a result of the inflammatory and oxidative stress. The network interaction also showed significant alterations in mitochondrial and neuronal cytoskeleton proteins as a result of chronic IL-6 expression.

Correlation of Motor Test Scores with Protein Spot Volumes

Pearson correlation (two-tailed) analysis was performed to assess whether average motor function scores of the WT and GFAP-IL6 mice in the elevated beam walking and accelerod tests were correlated to the average spot volume of each identified protein in their cerebelli. For this purpose, averaged 'number of footslips' and 'time to traverse' values in the beam walking test and averaged and best 'time to fall' values in the accelerod test were correlated to the spot volumes of the soluble and membrane proteins. The significant correlation results for WT and GFAP-IL6 mice together are shown in Table 2 and the rest of the results are shown in Supplementary Table S3. Averaged 'time to traverse' and 'number of footslips' scores of the mice were positively correlated to peroxiredoxin-6 ($p = 0.033$, $r = 0.848$ and $p = 0.030$, $r = 0.856$, respectively) and negatively correlated to α-internexin ($p = 0.004$, $r = -0.946$ and $p = 0.012$, $r = -0.911$) and mitochondrial cristae subunit Mic19 ($p = 0.026$, $r = -0.864$ and $p = 0.031$, $r = -0.853$, respectively). Also, averaged and best 'time to fall' scores of the mice were positively correlated to forkhead box protein K2 ($p = 0.012$, $r = 0.909$ and $p = 0.014$, $r = 0.901$, respectively).

Discussion

Summary of Key Findings

In this study, we assessed motor skills and subsequently analysed the cerebellar proteome of the GFAP-IL6 transgenic mice and compared them to the WT counterparts to examine the effects of IL-6-induced chronic inflammatory process in the cerebellum. The transgenic mice exhibited motor deficits in the walking beam test, whereas their accelerod test skills were not significantly different than the WT mice. Whole cerebellum proteomic analysis revealed significant changes in both membrane and soluble proteoforms which were associated with motor behavioural deficits, neurodegeneration, metabolism and protein aggregation. Comparison of the cerebellar proteome of the GFAP-IL6 and WT mice showed notable changes in the abundance of 47 soluble proteins and 20 membrane proteins. Also, 5 soluble proteins and one membrane protein were present only in the cerebellar proteome of the GFAP-IL6 mice while one membrane protein was found only in the WT mice proteome. These changes indicated increased response to oxidative stress and unfolded proteins, and upregulation of glycolytic process while a significant reduction in mitochondrial oxidative phosphorylation and altered neuronal cytoskeleton as a result of the chronic inflammation. The motor test scores of the mice were positively correlated to peroxiredoxin-6 and negatively correlated to mitochondrial cristae complex subunit Mic19 and α-internexin demonstrating prediction of motor function decline by these proteins.

Relationship Between Motor Behaviour and Changes in Cerebellum Proteome

The cerebellum is the brain region associated with controlling motor coordination, balance and inflammatory process in this region leads to deficits in motor function [41, 51]. In line with this, we also found the impaired motor performance of the GFAP-IL6 mice when measured their 'number of footslips' and 'time to traverse' scores. On the contrary, no significant differences were observed in the accelerod test which could be due to the higher sensitivity of the beam walking test for detecting motor deficits in mice as well as the influence of various parameters on accelerod test performance including rotarod diameter, rotation speed, pretraining and pharmacological treatment of animals [40, 52–55]. Furthermore, no significant difference was observed in body weights of the GFAP-IL6 mice when compared to the WT counterparts. This finding is intriguing as previously published study showed cerebellar neurodegeneration, motor

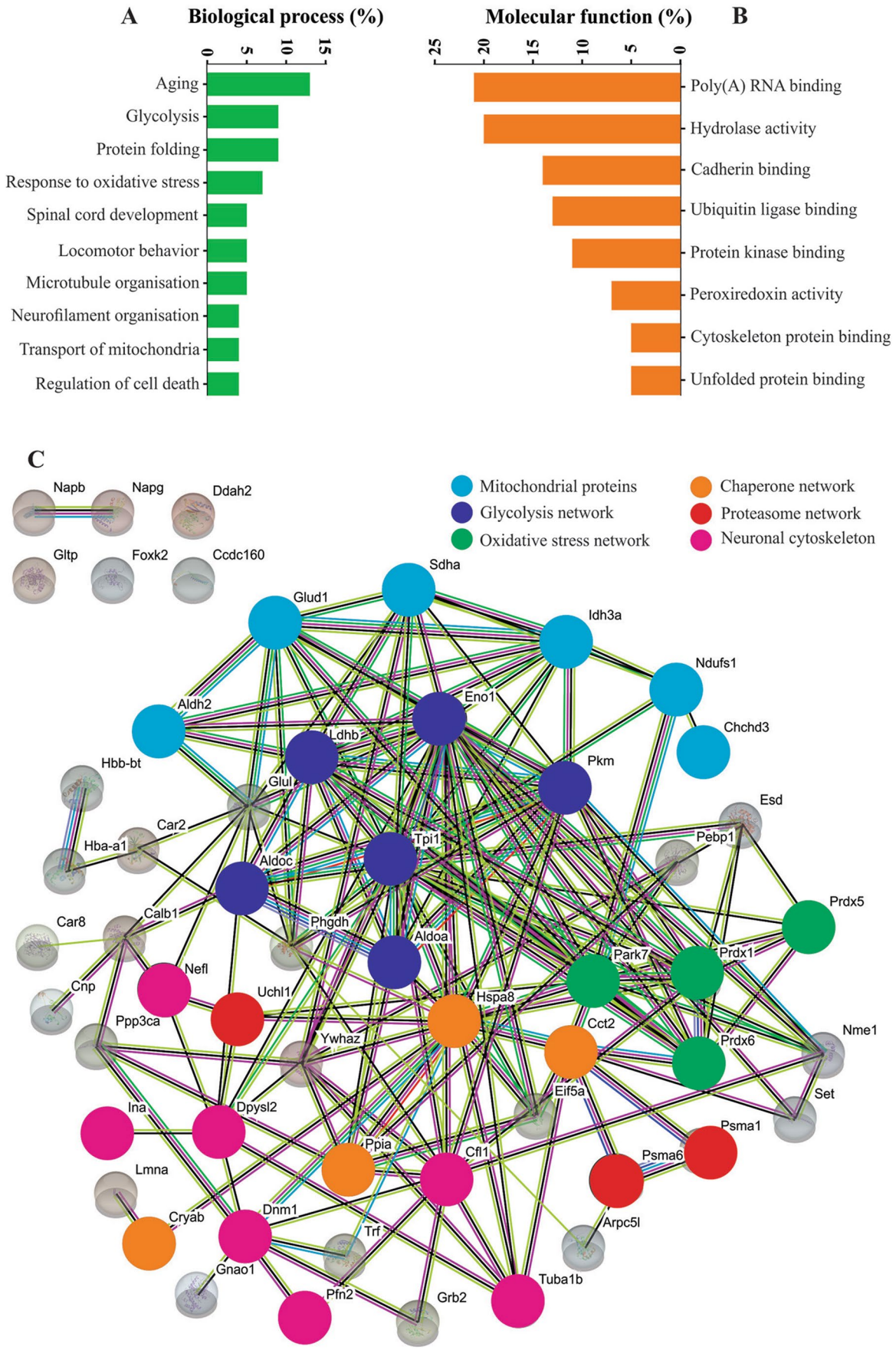
A
Biological process (%)
0
5
10
15
Aging
Glycolysis
Protein folding
Response to oxidative stress
Spinal cord development
Locomotor behavior
Microtubule organisation
Neurofilament organisation
Transport of mitochondria
Regulation of cell death
B
Molecular function (%)
25
20
15
10
5
0
Poly(A) RNA binding
Hydrolase activity
Cadherin binding
Ubiquitin ligase binding
Protein kinase binding
Peroxiredoxin activity
Cytoskeleton protein binding
Unfolded protein binding
C
Mitochondrial proteins
Glycolysis network
Oxidative stress network
Chaperone network
Proteasome network
Neuronal cytoskeleton
Napb
Napg
Ddah2
Gltp
Foxk2
Ccdc160
Sdha
Glud1
Idh3a
Ndufs1
Aldh2
Eno1
Chchd3
Ldhb
Hbb-bt
Pkm
Glul
Esd
Car2
Hba-a1
Tpi1
Pebp1
Aldoc
Prdx5
Calb1
Car8
Phgdh
Aldoa
Park7
Prdx1
Nefl
Cnp
Uchl1
Hspa8
Ppp3ca
Cct2
Nme1
Ywhaz
Prdx6
Eif5a
Set
Ina
Dpysl2
Psma1
Ppia
Cfl1
Psma6
Lmna
Cryab
Dnm1
Arpc5l
Trf
Gnao1
Tuba1b
Pfn2
Grb2

◂**Fig. 3** Functional annotation and network analysis of the identified proteins by DAVID and STRING bioinformatics tools. **A** DAVID analysis revealed proteins functional enrichment in biological processes such as ageing, glycolysis, protein folding, response to oxidative stress, spinal cord development, locomotor behaviour and regulation of cell death. **B** Their functions included (DAVID analysis) poly(A) RNA-binding, hydrolase activity, cadherin binding, ubiquitin-protein ligase binding, protein kinase binding, peroxiredoxin activity, cytoskeletal protein binding and unfolded protein binding. **C** Functional interactions of the proteins in the STRING analysis showed their network in the glycolytic process, peroxiredoxin, chaperone and proteasome systems, mitochondrial function and neuronal cytoskeleton organisation. The findings indicate IL-6 induced changes in molecular and cellular functions including regulation of RNA transcriptome, peroxiredoxin, chaperone and proteasomal activities, and alterations in glycolytic process, neuronal cytoskeleton and mitochondrial function. The thickness of the lines shows the strength of data support while lines of different colours indicate the type of interaction evidence. Known protein interactions are shown by light blue and purple lines while predicted interactions are shown by green, red and dark blue lines

impairment and reduced body weight development in mice with brain-specific chronic overexpression of another proinflammatory cytokine tumour necrosis factor-α (TNF-α) [56]. This could be due to sex-specific effects of cytokine-induced brain inflammation on body weight development in mice as demonstrated in another study [57]. In fact, decreased levels of brain IL-6 expression were found in obese male mice but not in obese female mice [58] indicating regulatory role of this cytokine but not IL-1 or TNF-α for normal bodyweight development in male organism. Central nervous system IL-6 levels were also associated with bodyweight function in male human subjects [59].

Although motor impairment of both male and female heterozygous GFAP-IL6 mice at 14 months of age was previously reported [1], for the first time, we attempted to examine cerebellar proteome changes underlying their motor deficits. For this purpose, the motor test scores of the mice were correlated to levels of the identified proteoforms in their cerebelli. We found a significant positive correlation of the beam walking scores of the mice to peroxiredoxin-6 and a negative correlation to alpha-internexin and mitochondrial cristae complex subunit Mic19 levels. Peroxiredoxin-6 plays an important role in cell membrane repair and integrity via its glutathione-dependent peroxidase function and its increased levels in the cerebelli of the GFAP-IL6 mice reflect an endogenous response to oxidative damage to neuronal and synaptic membranes [17, 60].

Significantly reduced levels of Mic19 subunit and alpha-internexin also displayed similar pathogenic changes in the cerebelli of the transgenic mice as these proteins play an essential role in mitochondrial cristae structure organisation and intermediate filament assembly in dendritic spines, respectively [61, 62]. These findings are also supported by previously published evidence demonstrating social memory deficits and significantly reduced long-term potentiation (LTP) in the hippocampal Schaffer collateral pathway of transgenic mice with knockout of alpha-internexin, neurofilament heavy and light polypeptides [63].

On the other hand, the Mic19 subunit was found to play an essential role in the interaction of MICOS (mitochondrial contact site and cristae organising system) subcomplexes as well as regulate their number and positional distribution to the inner mitochondrial membrane thereby determining inner membrane architecture [64]. Loss of MICOS complex integrity and mitochondrial damage was found to cause severe motor neuron disease in patients with frontotemporal dementia–amyotrophic lateral sclerosis clinical spectrum [65]. Impaired mitochondrial cristae were also shown as part of pathoetiology in hereditary sensory neuropathy, a disease characterised by axonal degeneration in afflicted patients [66]. The negative correlation of averaged 'time to traverse' and 'number of footslips' of the mice to alpha-internexin and Mic19 levels in our study suggests these proteins could be potential biomarkers for prognosis of motor function decline. The functional effects of the proteome changes were also indicated by significant positive correlation of the averaged 'time to fall' scores to the forkhead box protein K2 levels which are in line with findings of a previous study showing induction of aerobic glycolysis and inhibition of citric acid cycle metabolism by this transcription factor in mice subjected to physical exercise [67].

The proteome of the GFAP-IL6 mice displayed significant alteration in a network of neuronal cytoskeleton proteins including tubulin, neurofilament, cofilin-1 and profilin-2 which suggests injury to neuro-architecture and deterioration of neuronal communication leading to their motor decline [68, 69]. IL-6-induced chronic inflammatory damage to neurons was also seen by significantly reduced levels of calbindin protein, a Purkinje cell marker indicating loss of these neurons in the cerebelli of the GFAP-IL6 mice which explain their tremor and limb errors seen in our current study using the beam walking test [41, 70]. Degeneration and loss of calbindin-positive Purkinje neurons in GFAP-IL6 mice cerebelli are confirmed in a study recently published by our group [71].

The Proteome Changes Linked to Inflammation and Neurodegeneration

It is noteworthy to highlight that IL-6 can play both toxic and neuroprotective roles depending on the microenvironment and surrounding glial cell population in the brain [72]. Previously published results by our group clearly showed increased microglia and astrocyte activation in the cerebellum region of the GFAP-IL6 mice using inflammation-specific markers and showing significant morphological changes in soma and processes of the cells [16]. GFAP-IL6 mice were also

Table 2 Pearson correlation (PC) of the average scores of motor tests to the cerebellar spot volumes of the proteins. Correlation of the average scores of 'time to traverse', 'number of footslips', average and best scores of 'time to fall' of the WT and GFAP-IL6 mice (n = 6) to the spot volumes of their cerebellar soluble and membrane proteins. *PC* Pearson correlation, *Sig* significance (2-tailed, $P < 0.05$). Numbers in bold represent a significant value in each category

		Elevated beam walking		Accelerod	
Protein	PC/sig	Time to traverse (average score)	Number of footslips (average score)	Time to fall (average score)	Time to fall (best score)
Prdx6	PC	0.848	0.856	0.370	0.345
	Sig	**0.033**	**0.030**	0.470	0.503
Ainx	PC	−0.946	−0.911	−0.207	−0.103
	Sig	**0.004**	**0.012**	0.693	0.846
Mic19	PC	−0.864	- 0.853	−0.281	−0.237
	Sig	**0.026**	**0.031**	0.590	0.651
Foxk2	PC	0.503	0.503	0.909	0.901
	Sig	0.310	0.309	**0.012**	**0.014**

characterised by pathological deposition of iron in their cerebellar region [17] which explains increased serotransferrin levels in the transgenic group of this study [73].

IL-6 is a multifunctional cytokine and its signalling occurs through two different receptor types, classic signalling via a membrane-bound receptor and trans-signalling through its soluble receptor [72, 74]. The trans-signalling was previously shown responsible for most of the inflammatory and neurodegenerative effects of the cytokine in the cerebellum region including glial cell activation, vasculopathy, blood–brain barrier breakdown and impaired neurogenesis [75]. Interestingly, recently published study results demonstrated the role of repopulated microglia in promoting neuroprotection and neurogenesis which was critically dependent on IL-6 trans-signalling in a mouse model with acute brain injury and ensuing inflammation [76]. Another study also reported enhanced inflammatory reaction in the brain stem of the GFAP-IL6 mice with acute chemical agent-induced toxicity to neuroglia and expression of IL-6 was neuroprotective by promoting angiogenesis and reducing oxidative stress and apoptotic cell death [77]. This could be explained by the fact that IL-6 signalling exerts protective actions in the brain particularly under conditions of acute injury and toxicity [78, 79]. Moreover, microglia may become activated and take distinct functional phenotypes depending on the brain region, the form of acute injury or chronic disease condition as suggested in previous studies [80, 81]. Therefore, microenvironment and glial cell heterogeneity could determine differential effects for IL-6 trans-signalling. The role of IL-6 signalling in the brain has been also elucidated by studies of IL-6 knockout mice. Transgenic mice with deletion of IL-6 gene was reported with significantly reduced neurogenesis and compromised inflammatory response and neuroprotection following traumatic brain injury [82, 83]. Interestingly, behavioural phenotype of IL-6 knockout mice was reported to involve resistance to depressive-like behaviour induced by stress, impaired object recognition and better radial maze learning compared to WT counterparts [84–86].

In our study, IL-6-induced inflammatory reaction was characterised by significantly increased expression of glial fibrillary acidic protein which co-migrated with peroxiredoxin-6 (S2, Supplementary Excel file) and heat shock cognate 71-kD protein (S33, Supplementary Excel file) to the same location in the 2D gels with 16 and 18 uniquely detected peptides and 480 and 2632 PLGS scores, respectively. GFAP is a marker of activated astrocytes and its increased abundance in the GFAP-IL6 mice cerebelli demonstrates astroglial activation in their brains as shown in our previous study [16]. The findings of that study showed increased expression of GFAP as a result of chronic neuroinflammation in GFAP-IL6 mice [16].

It should be noted that protein interaction analysis using DAVID and STRING online bioinformatics tools did not reveal inflammatory network for the identified proteins but showed their network in glucose metabolism, oxidative stress response, chaperone and ubiquitin proteasomal systems. In this line, current findings also did not reveal proteins specifically involved in proliferative angiopathy as shown in the original study of the GFAP-IL6 model. It could be explained by the fact that mammalian proteome such as one derived from mouse cerebellar region presents high-level complexity and variety in composition considering proteoforms' wide range physicochemical properties, abundance, complexation, isoforms and post-translational modifications [87]. Therefore, it is not possible to resolve the entire cerebellar proteome using single sample preparation and protein separation protocol. For instance, GFAP-IL6 mice were reported with proliferative angiopathy in their cerebelli using immunolabeling for the von Willebrand factor (vWF) [14]. However, we did not identify this protein in our study as its 309-kD molecular weight lied outside the upper limit of resolution in our current 2-DE analysis [88]. The absence of an inflammatory

network could be also due to adaptive alterations at the age of analysis in this study compared to the postnatal findings of GFAP-IL6 mice in the original study [14]. For example, we found significantly reduced levels of eukaryotic translation initiation factor 5A-1 in the transgenic mice which is a mediator for the post-transcriptional synthesis of several pro-inflammatory mediators including iNOS, IL-1 and IL-6 [89, 90]. Reduced levels of this translation initiation factor may have resulted in decreased levels of inflammatory network proteins in the current study. This finding also emphasises the importance of longitudinal analysis of the cerebellar proteome of GFAP-IL6 mice to better understand the chronology of IL-6-induced pathophysiology and discover proteome correlates underlying their functional impairment and neurological disease which develop at 6 months of age as reported in the original study [14].

The Proteome Changes Linked to Glucose Metabolism

Glucose is the primary source for cellular ATP energy production in the brain via a series of enzymatic reactions in the cytoplasm and subsequent oxidative phosphorylation in mitochondria [91]. Previous studies have shown that inflammatory challenges observed in neurodegenerative conditions may lead to alterations in energy metabolism by stimulating glycolysis while causing deficits in oxidative phosphorylation [92–94]. This phenomenon was also evident in the GFAP-IL6 mice proteome which showed increased levels of glycolytic enzymes including fructose-bisphosphate aldolase, triosephosphate isomerase and alpha-enolase while reduced levels of pyruvate kinase and isocitrate dehydrogenase essential enzymes for the citric acid cycle and generation of electron carriers for oxidative phosphorylation in mitochondria [95]. These findings suggest metabolic disturbance and mitochondrial alteration in the GFAP-IL6 mice as seen in AD patients [96, 97].

GFAP-IL6 Mice Proteome Linked to Protein Aggregation

We have previously shown chronic neuroinflammation in GFAP-IL6 mice [1, 16], but this is the first study that revealed protein aggregation-related proteins in this mouse model. Several chaperones including heat shock cognate 71-kD protein were detected. They are a ubiquitous family of enzymes and regulate protein folding and assembly [98], which suggests an increase in unfolded protein response and protein self-aggregation. The identified proteoforms were also associated with ubiquitin proteasomal networks (ubiquitin carboxyl-terminal hydrolase isozyme L1) which were closely linked to oxidative stress response and this reflects sequelae of molecular mechanisms activated by IL-6-initiated inflammatory cascade. These proteins play an essential neuroprotective role in the repair or degradation of misfolded protein aggregates formed during the neurodegenerative process [99, 100]. However, chronic inflammation can lead to dysregulation of these networks by overloading cellular capacity with aberrant aggregates or inhibition of proteasomal activity [101, 102]. The evidence from previous studies showed a direct link between chaperone proteins heat shock 70/90 and proteasomal machinery to degrade ubiquitin-tagged protein aggregates followed by protein misfolding [103]. The GFAP-IL6 mice proteome displayed a significantly increased level of heat shock protein 70 and de novo expression of heat shock protein 90 suggesting probable interaction of these mechanisms in their cerebelli. These findings are similar to histopathology of neurodegenerative diseases with ubiquitin immunoreactive protein aggregates in the brain suggesting failed or dysregulated proteasome mechanisms in the course of these diseases [104, 105].

Post-translational Modifications Induced by Chronic IL-6 Expression

The present analysis detected few proteoforms, in both soluble and membrane fractions with different experimental MW and pI values. These included dihydropyrimidinase-related protein 2, heat shock cognate 71-kD protein, l-lactate dehydrogenase B chain, peroxiredoxin-6, profilin-2, triosephosphate isomerase and tubulin alpha-1B chain (Table 1). This could be due to the PTMs of these proteoforms resulting in differential migration during separation as revealed by various modifications of tubulins in different neuronal compartments [106]. In our study, heat shock cognate 71-kD protein and peroxiredoxin-6 were found by an increased abundance from both soluble and membrane fractions. The increased levels may be contributed by the release of heat shock protein 70 from astroglia to the extracellular environment which protects neuronal cells from stress-induced apoptosis [107, 108]. Distinct enzymatic functions of peroxiredoxin-6 are dependent on its subcellular localisation and PTMs can change these activities by mediating intracellular localisation of the peroxidase [60, 109]. Phosphorylation of peroxiredoxin-6 by mitogen-activated protein kinase (MAPK) has been previously shown to target the peroxiredoxin to membrane-bound lysosomal organelles [110].

Limitations of This Study and Future Research Work

Chronic IL-6-induced inflammatory alterations in the cerebellar proteins of the GFAP-IL6 mice have been also confirmed by immunohistochemical evidence recently published by our group in peer-reviewed journals. These

include studies showing significant atrophy and loss of calbindin-positive Purkinje neurons in the cerebellar region of GFAP-IL6 mice at 12 and 24 months of age ($P < 0.0001$ and $P < 0.001$, respectively) [71] and increased expression of activated astrocyte marker GFAP in GFAP-IL6 mice cerebelli at 8 months of age compared to age-matched WT mice [16]. However, additional experimental work is needed to better understand mechanisms underlying cerebellar histopathology and motor function deficits of the GFAP-IL6 mice. For this purpose, future research studies should aim for validation of the current proteome findings using immunohistochemistry, western blot and cell culture assays as well as examine proteome analysis of GFAP-IL6 mice at an earlier age time point and targeted validation of the poorly resolved proteins and PTMs using PTM-based staining (e.g. phospho and glycol) [111]. The findings may potentially lead to the discovery of novel protein targets for effective therapeutics of brain inflammatory diseases.

Conclusions

This study showed that IL-6 overexpression in the brain leads to motor behavioural deficits that were only evident when a complex behavioural task was used. The current study also revealed for the first time that lack of fine motor control is closely associated with the proteoform changes in the cerebellum. The identified cerebellar proteoforms were associated with the metabolic and cellular responses to oxidative stress, mitochondrial structural integrity and function, and neuronal cytoskeleton organisation, suggesting the multifactorial nature of GFAP-IL6 pathobiology. The functional network of the identified proteoforms revealed molecular sequelae of pathophysiological changes underlying IL-6-induced neurological disease of the GFAP-IL6 mice.

Supplementary Information The online version contains supplementary material available at https://doi.org/10.1007/s12311-021-01303-1.

Acknowledgements We are grateful to the Animal Facility and Mass Spectrometry Facility for their help with this project.

Author Contribution Experimental work and data analysis was carried out by RA. RA and MKS wrote the manuscript. TK, EG, CM and GM conceived and designed the experiments. DM, CM, EG and GM revised the manuscript. CM and MM helped with mass spectrometry analysis. All authors approved the final version of the manuscript.

Funding This work was funded by the Western Sydney University Ph.D. scholarship RTP expenditure fund. RA was the recipient of WSU International Postgraduate Research Scholarship. TK receives funding from two project grants from the National Health and Medical Research Council [#1102012 and #1141789] and the NHMRC dementia research team initiative [#1095215] as well as the Ainsworth Medical Research Innovation Fund and the Australian Research Council [#DP18010473].

Declarations

Conflict of Interest The authors declare no competing interests.

References

1. Gyengesi E, Rangel A, Ullah F, Liang H, Niedermayer G, Asgarov R, Venigalla M, Gunawardena D, Karl T, Munch G. Chronic microglial activation in the GFAP-IL6 mouse contributes to age-dependent cerebellar volume loss and impairment in motor function. Front Neurosci. 2019;13:303.
2. Walker KA. Inflammation and neurodegeneration: chronicity matters. Aging. 2018;11(1):3–4.
3. Chitnis T, Weiner HL. CNS inflammation and neurodegeneration. J Clin Invest. 2017;127(10):3577–87.
4. Gyengési E, Muench G. In search of an anti-inflammatory drug for Alzheimer disease. Nat Rev Neurol. 2020;16(3):131–2.
5. DiSabato DJ, Quan N, Godbout JP. Neuroinflammation: the devil is in the details. J Neurochem. 2016;139:136–53.
6. Morales I, Guzmán-Martínez L, Cerda-Troncoso C, Farías GA, Maccioni RB. Neuroinflammation in the pathogenesis of Alzheimer's disease. A rational framework for the search of novel therapeutic approaches. Front Cell Neurosci 2014;8:(112).
7. Godbout JP, Johnson RW. Interleukin-6 in the aging brain. J Neuroimmunol. 2004;147(1):141–4.
8. Huell M, Strauss S, Volk B, Berger M, Bauer J. Interleukin-6 is present in early stages of plaque formation and is restricted to the brains of Alzheimer's disease patients. Acta Neuropathol. 1995;89(6):544–51.
9. Hüll M, Fiebich BL, Lieb K, Strauss S, Berger M, Volk B, Bauer J. Interleukin-6-associated inflammatory processes in Alzheimer's disease: new therapeutic options. Neurobiol Aging. 1996;17(5):795–800.
10. Bettcher BM, Watson CL, Walsh CM, Lobach IV, Neuhaus J, Miller JW, Green R, Patel N, Dutt S, Busovaca E, et al. Interleukin-6, age, and corpus callosum integrity. PLoS One 2014;9(9):e106521.
11. Singh-Manoux A, Dugravot A, Brunner E, Kumari M, Shipley M, Elbaz A, Kivimaki M. Interleukin-6 and C-reactive protein as predictors of cognitive decline in late midlife. Neurol. 2014;83(6):486–93.
12. Quintanilla RA, Orellana DI, González-Billault C, Maccioni RB. Interleukin-6 induces Alzheimer-type phosphorylation of tau protein by deregulating the cdk5/p35 pathway. Exp Cell Res. 2004;295(1):245–57.
13. Gruol DL, Nelson TE. Purkinje neuron physiology is altered by the inflammatory factor interleukin-6. Cerebellum. 2005;4(3):198–205.
14. Campbell IL, Abraham CR, Masliah E, Kemper P, Inglis JD, Oldstone MB, Mucke L. Neurologic disease induced in transgenic mice by cerebral overexpression of interleukin 6. Proc Natl Acad Sci. 1993;90(21):10061–5.
15. Chiang CS, Stalder A, Samimi A, Campbell IL. Reactive gliosis as a consequence of interleukin-6 expression in the brain: studies in transgenic mice. Develop Neurosci. 1994;16(3–4):212–21.
16. Ullah F, Asgarov R, Venigalla M, Liang H, Niedermayer G, Münch G, Gyengesi E. Effects of a solid lipid curcumin particle formulation on chronic activation of microglia and astroglia in the GFAP-IL6 mouse model. Sci Rep. 2020;10(1):2365.
17. Castelnau PA, Garrett RS, Palinski W, Witztum JL, Campbell IL, Powell HC. Abnormal iron deposition associated with lipid

peroxidation in transgenic mice expressing interleukin-6 in the brain. J Neuropathol Exp Neurol. 1998;57(3):268–82.
18. Heyser CJ, Masliah E, Samimi A, Campbell IL, Gold LH. Progressive decline in avoidance learning paralleled by inflammatory neurodegeneration in transgenic mice expressing interleukin 6 in the brain. Proc Natl Acad Sci. 1997;94(4):1500–5.
19. Coorssen JR, Yergey AL. Proteomics is analytical chemistry: fitness-for-purpose in the application of top-down and bottom-up analyses. Proteome. 2015;3(4):440–53.
20. Shevchenko G, Konzer A, Musunuri S, Bergquist J. Neuroproteomics tools in clinical practice. BBA. 2015;1854(7):705–17.
21. Hanash S. Disease proteomics. Nat. 2003;422(6928):226–32.
22. Fasano M, Monti C, Alberio T. A systems biology-led insight into the role of the proteome in neurodegenerative diseases. Expert Rev Proteomics. 2016;13(9):845–55.
23. Davidsson P, Sjögren M. The use of proteomics in biomarker discovery in neurodegenerative diseases. Dis Markers. 2005;21(2):81–92.
24. Anderson NL, Anderson NG. Proteome and proteomics: new technologies, new concepts, and new words. Electrophoresis. 1998;19(11):1853–61.
25. Sen MK, Almuslehi MSM, Gyengesi E, Myers SJ, Shortland PJ, Mahns DA, Coorssen JR. Suppression of the peripheral immune system limits the central immune response following cuprizone-feeding: relevance to modelling multiple sclerosis. Cells. 2019;8(11):1314.
26. Butterfield DA. Proteomics: a new approach to investigate oxidative stress in Alzheimer's disease brain. Brain Res. 2004;1000(1):1–7.
27. Wright EP, Partridge MA, Padula MP, Gauci VJ, Malladi CS, Coorssen JR. Top-down proteomics: enhancing 2D gel electrophoresis from tissue processing to high-sensitivity protein detection. Proteomics. 2014;14(7–8):872–89.
28. Görg A, Boguth G, Obermaier C, Posch A, Weiss W. Two-dimensional polyacrylamide gel electrophoresis with immobilized pH gradients in the first dimensin (IPG-Dalt): the state of the art and the controversy of vertical versus horizontal systems. Electrophoresis. 1995;16(1):1079–86.
29. Gorg A, Weiss W, Dunn MJ. Current two-dimensional electrophoresis technology for proteomics. Proteomics. 2004;4(12):3665–85.
30 Görg A, Postel W, Günther S. Two-dimensional electrophoresis. The current state of two-dimensional electrophoresis with immobilized pH gradients. Electrophoresis 1988;9(9):531–546.
31. Gorg A, Drews O, Luck C, Weiland F, Weiss W. 2-DE with IPGs. Electrophoresis. 2009;30:122–32.
32. Bjellqvist B, Ek K, Righetti PG, Gianazza E, Gorg A, Westermeier R, Postel W. Isoelectric focusing in immobilized pH gradients: principle, methodology and some applications. J Biochem Biophys Methods. 1982;6(4):317–39.
33. Diedrich M, Kitada T, Nebrich G, Koppelstaetter A, Shen J, Zabel C, Klose J, Mao L. Brain region specific mitophagy capacity could contribute to selective neuronal vulnerability in Parkinson's disease. Proteome Sci. 2011;9:59–59.
34. Burgula S, Medisetty R, Jammulamadaka N, Musturi S, Ilavazhagan G, Singh SS. Downregulation of PEBP1 in rat brain cortex in hypoxia. J Mol Neurosci. 2010;41(1):36–47.
35. Joerchel S, Raap M, Bigl M, Eschrich K, Schliebs R. Oligomeric beta-amyloid(1–42) induces the expression of Alzheimer disease-relevant proteins in cholinergic SN56.B5.G4 cells as revealed by proteomic analysis. Int J Dev Neurosci 2008;26(3–4):301–308.
36. Aebersold R, Mann M. Mass spectrometry-based proteomics. Nat. 2003;422(6928):198–207.
37 Mishra NC, Blobel G, Blobel G. Nter: Introduction to Proteomics: Principles and Applications. Hoboken: John Wiley & Sons, Incorporated; 2010.
38. Deacon RM. Housing, husbandry and handling of rodents for behavioral experiments. Nat Protoc. 2006;1(2):936–46.
39. Fridgeirsdottir GA, Hillered L, Clausen F. Escalated handling of young C57BL/6 mice results in altered Morris water maze performance. Upsala J Med Sci. 2014;119(1):1–9.
40. Sen MK, Mahns DA, Coorssen JR, Shortland PJ. Behavioural phenotypes in the cuprizone model of central nervous system demyelination. Neurosci Biobehav Rev. 2019;107:23–46.
41. Sen MK, Almuslehi MSM, Coorssen JR, Mahns DA, Shortland PJ. Behavioural and histological changes in cuprizone-fed mice. Brain Behav Immun. 2020;87:508–23.
42. Carter RJ, Morton J, Dunnett SB: Motor coordination and balance in rodents. Curr Protoc Neurosci 2001;Chapter 8:Unit 8.12.
43. Southwell AL, Ko J, Patterson PH. Intrabody gene therapy ameliorates motor, cognitive, and neuropathological symptoms in multiple mouse models of Huntington's disease. J Neurosci. 2009;29(43):13589–602.
44. Butt RH, Coorssen JR. Postfractionation for enhanced proteomic analyses: routine electrophoretic methods increase the resolution of standard 2D-PAGE. J Proteome Res. 2005;4(3):982–91.
45. Churchward MA, Butt RH, Lang JC, Hsu KK, Coorssen JR. Enhanced detergent extraction for analysis of membrane proteomes by two-dimensional gel electrophoresis. Proteome Sci. 2005;3(1):5–5.
46. Agnew BJ, Murray D, Patton WF. A rapid solid-phase fluorescence-based protein assay for quantitation of protein electrophoresis samples containing detergents, chaotropes, dyes, and reducing agents. Electrophoresis. 2004;25(15):2478–85.
47. Stimpson SE, Coorssen JR, Myers SJ. Mitochondrial protein alterations in a familial peripheral neuropathy caused by the V144D amino acid mutation in the sphingolipid protein, SPTLC1. J Chem Biol. 2015;8(1):25–35.
48. Wright EP, Prasad KA, Padula MP, Coorssen JR. Deep imaging: how much of the proteome does current top-down technology already resolve? PLoS One 2014;9(1):e86058.
49. Huang DW, Sherman BT, Tan Q, Kir J, Liu D, Bryant D, Guo Y, Stephens R, Baseler MW, Lane HC, et al. DAVID Bioinformatics Resources: expanded annotation database and novel algorithms to better extract biology from large gene lists. Nucleic Acids Res 2007;35:W169–175.
50. Sherman BT, Huang DW, Tan Q, Guo Y, Bour S, Liu D, Stephens R, Baseler MW, Lane HC, Lempicki RA. DAVID Knowledgebase: a gene-centered database integrating heterogeneous gene annotation resources to facilitate high-throughput gene functional analysis. BMC Bioinformatics. 2007;8(1):426.
51. Anderson ME. The role of the cerebellum in motor control and motor learning. Phys Med Rehabil Clin N Am. 1993;4(4):623–36.
52. Rozas G, Guerra MJ, Labandeira-Garcia JL. An automated rotarod method for quantitative drug-free evaluation of overall motor deficits in rat models of parkinsonism. Brain Res Protoc. 1997;2(1):75–84.
53. Rustay NR, Wahlsten D, Crabbe JC. Influence of task parameters on rotarod performance and sensitivity to ethanol in mice. Behav Brain Res. 2003;141(2):237–49.
54. Shiotsuki H, Yoshimi K, Shimo Y, Funayama M, Takamatsu Y, Ikeda K, Takahashi R, Kitazawa S, Hattori N. A rotarod test for evaluation of motor skill learning. J Neurosci Methods. 2010;189(2):180–5.
55. Stanley JL, Lincoln RJ, Brown TA, McDonald LM, Dawson GR, Reynolds DS. The mouse beam walking assay offers improved sensitivity over the mouse rotarod in determining motor coordination deficits induced by benzodiazepines. J Psychopharmacol. 2005;19(3):221–7.
56. Probert L, Akassoglou K, Pasparakis M, Kontogeorgos G, Kollias G. Spontaneous inflammatory demyelinating disease

in transgenic mice showing central nervous system-specific expression of tumor necrosis factor alpha. Proc Natl Acad Sci. 1995;92(24):11294–8.
57. Bolton JL, Smith SH, Huff NC, Gilmour MI, Foster WM, Auten RL, Bilbo SD. Prenatal air pollution exposure induces neuroinflammation and predisposes offspring to weight gain in adulthood in a sex-specific manner. FASEB J. 2012;26(11):4743–54.
58. Mishra D, Richard JE, Maric I, Porteiro B, Häring M, Kooijman S, Musovic S, Eerola K, López-Ferreras L, Peris E, et al. Parabrachial interleukin-6 reduces body weight and food intake and increases thermogenesis to regulate energy metabolism. Cell Rep 2019;26(11):3011-3026.e5.
59. Stenlöf K, Wernstedt I, Fjällman T, Wallenius V, Wallenius K, Jansson JO. Interleukin-6 levels in the central nervous system are negatively correlated with fat mass in overweight/obese subjects. J Clin Endocrinol Metab. 2003;88(9):4379–83.
60. Arevalo JA, Vázquez-Medina JP. The role of peroxiredoxin 6 in cell signaling. Antioxidants. 2018;7(12):172.
61. Benson DL, Mandell JW, Shaw G, Banker G. Compartmentation of alpha-internexin and neurofilament triplet proteins in cultured hippocampal neurons. J Neurocytol. 1996;25(1):181–96.
62. Kozjak-Pavlovic V. The MICOS complex of human mitochondria. Cell Tissue Res. 2017;367(1):83–93.
63. Yuan A, Sershen H, Veeranna, Basavarajappa BS, Kumar A, Hashim A, Berg M, Lee JH, Sato Y, Rao MV, et al. Neurofilament subunits are integral components of synapses and modulate neurotransmission and behavior in vivo. Mol Psychiatry 2015;20(8):986–994.
64 Friedman JR, Mourier A, Yamada J, McCaffery JM, Nunnari J. MICOS coordinates with respiratory complexes and lipids to establish mitochondrial inner membrane architecture. eLife 2015;4:e07739.
65. Genin EC, Bannwarth S, Lespinasse F, Ortega-Vila B, Fragaki K, Itoh K, Villa E, Lacas-Gervais S, Jokela M, Auranen M, et al. Loss of MICOS complex integrity and mitochondrial damage, but not TDP-43 mitochondrial localisation, are likely associated with severity of CHCHD10-related diseases. Neurobiol Dis. 2018;119:159–71.
66. Myers SJ, Malladi CS, Hyland RA, Bautista T, Boadle R, Robinson PJ, Nicholson GA. Mutations in the SPTLC1 protein cause mitochondrial structural abnormalities and endoplasmic reticulum stress in lymphoblasts. DNA Cell Biol. 2014;33(7):399–407.
67. Sukonina V, Ma H, Zhang W, Bartesaghi S, Subhash S, Heglind M, Foyn H, Betz MJ, Nilsson D, Lidell ME, et al. FOXK1 and FOXK2 regulate aerobic glycolysis. Nat. 2019;566(7743):279–83.
68. Fox GB, Faden AI. Traumatic brain injury causes delayed motor and cognitive impairment in a mutant mouse strain known to exhibit delayed wallerian degeneration. J Neurosci Res. 1998;53(6):718–27.
69. Hill CS, Coleman MP, Menon DK. Traumatic Axonal injury: mechanisms and translational opportunities. Trends Neurosci. 2016;39(5):311–24.
70. Kiyosawa K, Mokuno K, Murakami N, Yasuda T, Kume A, Hashizume Y, Takahashi A, Kato K. Cerebrospinal fluid 28-kDa calbindin-D as a possible marker for Purkinje cell damage. J Neurol Sci. 1993;118(1):29–33.
71. Childs R, Gamage R, Munch G, Gyengesi E. The effect of aging and chronic microglia activation on the morphology and numbers of the cerebellar Purkinje cells. Neurosci Letters. 2021;751:135807.
72. Spooren A, Kolmus K, Laureys G, Clinckers R, De Keyser J, Haegeman G, Gerlo S. Interleukin-6, a mental cytokine. Brain Res Rev. 2011;67(1):157–83.
73. Chiou B, Neely EB, Mcdevitt DS, Simpson IA, Connor JR. Transferrin and H-ferritin involvement in brain iron acquisition during postnatal development: impact of sex and genotype. J Neurochem. 2020;152(3):381–96.
74. Rose-John S, Scheller J, Elson G, Jones SA. Interleukin-6 biology is coordinated by membrane-bound and soluble receptors: role in inflammation and cancer. J Leukoc Biol. 2006;80(2):227–36.
75. Campbell IL, Erta M, Lim SL, Frausto R, May U, Rose-John S, Scheller J, Hidalgo J. Trans-signaling is a dominant mechanism for the pathogenic actions of interleukin-6 in the brain. J Neurosci. 2014;34(7):2503–13.
76. Willis EF, MacDonald KPA, Nguyen QH, Garrido AL, Gillespie ER, Harley SBR, Bartlett PF, Schroder WA, Yates AG, Anthony DC, et al. Repopulating Microglia promote brain repair in an IL-6-dependent manner. Cell 2020;180(5):833-846.e16.
77. Penkowa M, Camats J, Hadberg H, Quintana A, Rojas S, Giralt M, Molinero A, Campbell IL, Hidalgo J. Astrocyte-targeted expression of interleukin-6 protects the central nervous system during neuroglial degeneration induced by 6-aminonicotinamide. J Neurosci Res. 2003;73(4):481–96.
78. Loddick SA, Turnbull AV, Rothwell NJ. Cerebral interleukin-6 is neuroprotective during permanent focal cerebral ischemia in the rat. J Cereb Blood Flow Metab. 1998;18(2):176–9.
79. Toulmond S, Vige X, Fage D, Benavides J. Local infusion of interleukin-6 attenuates the neurotoxic effects of NMDA on rat striatal cholinergic neurons. Neurosci Letters. 1992;144(1–2):49–52.
80 Bachiller S, Jiménez-Ferrer I, Paulus A, Yang Y, Swanberg M, Deierborg T, Boza-Serrano A. Microglia in neurological diseases: a road map to brain-disease dependent-inflammatory response. Front Cell Neurosci 2018;12:488.
81 Hanisch U-K. Functional diversity of microglia – how heterogeneous are they to begin with? Front Cell Neurosci 2013;7:65.
82. Bowen KK, Dempsey RJ, Vemuganti R. Adult interleukin-6 knockout mice show compromised neurogenesis. Neuroreport. 2011;22(3):126–30.
83. Penkowa M, Moos T, Carrasco J, Hadberg H, Molinero A, Bluethmann H, Hidalgo J. Strongly compromised inflammatory response to brain injury in interleukin-6-deficient mice. Glia. 1999;25(4):343–57.
84. Braida D, Sacerdote P, Panerai AE, Bianchi M, Aloisi AM, Iosuè S, Sala M. Cognitive function in young and adult IL (interleukin)-6 deficient mice. Behav Brain Res. 2004;153(2):423–9.
85. Chourbaji S, Urani A, Inta I, Sanchis-Segura C, Brandwein C, Zink M, Schwaninger M, Gass P. IL-6 knockout mice exhibit resistance to stress-induced development of depression-like behaviors. Neurobiol Dis. 2006;23(3):587–94.
86. Hryniewicz A, Bialuk I, Kamiński KA, Winnicka MM. Impairment of recognition memory in interleukin-6 knock-out mice. Eur J Pharmacol. 2007;577(1–3):219–20.
87. Garbis S, Lubec G, Fountoulakis M. Limitations of current proteomics technologies. J Chromatogr A. 2005;1077(1):1–18.
88. Chitta MS, Duhé RJ, Kermode JC. Cloning of the cDNA for murine von Willebrand factor and identification of orthologous genes reveals the extent of conservation among diverse species. Platelets. 2007;18(3):182–98.
89. Maier B, Tersey SA, Mirmira RG. Hypusine: a new target for therapeutic intervention in diabetic inflammation. Discov Med. 2010;10(50):18–23.
90. Moore CC, Martin EN, Lee G, Taylor C, Dondero R, Reznikov LL, Dinarello C, Thompson J, Scheld WM. Eukaryotic translation initiation factor 5A small interference RNA-liposome complexes reduce inflammation and increase survival in murine models of severe sepsis and acute lung injury. J Infect Dis. 2008;198(9):1407–14.

91. Mergenthaler P, Lindauer U, Dienel GA, Meisel A. Sugar for the brain: the role of glucose in physiological and pathological brain function. Trends Neurosci. 2013;36(10):587–97.
92. Giri S, Suhail H, Singh J, Kumar A, Rattan R. Early burst of glycolysis in microglia regulates mitochondrial dysfunction in oligodendrocytes under neuro-inflammation. J Immunol 2018;200:49.16.
93. Jayasena T, Poljak A, Braidy N, Smythe G, Raftery M, Hill M, Brodaty H, Trollor J, Kochan N, Sachdev P. Upregulation of glycolytic enzymes, mitochondrial dysfunction and increased cytotoxicity in glial cells treated with Alzheimer's disease plasma. PloS One 2015;10(3):e0116092.
94. Rhein V, Song X, Wiesner A, Ittner LM, Baysang G, Meier F, Ozmen L, Bluethmann H, Dröse S. Brandt U et al. Amyloid-β and tau synergistically impair the oxidative phosphorylation system in triple transgenic Alzheimer's disease mice. Proc Natl Acad Sci. 2009;106(47):20057–62.
95. Nelson DL, Cox MM, Lehninger AL: Lehninger Principles of Biochemistry; 2017. 5th Edition p527-568.
96. Moreira PI, Carvalho C, Zhu X, Smith MA, Perry G. Mitochondrial dysfunction is a trigger of Alzheimer's disease pathophysiology. BBA. 2010;1802(1):2–10.
97. Swerdlow RH. Mitochondria and mitochondrial cascades in Alzheimer's disease. J Alzheimers Dis. 2018;62(3):1403–16.
98. Ellis RJ. The molecular chaperone concept. Semin Cell Biol. 1990;1(1):1–9.
99. Huang Q, Figueiredo-Pereira ME. Ubiquitin/proteasome pathway impairment in neurodegeneration: therapeutic implications. Apoptosis. 2010;15(11):1292–311.
100. van Noort J. Stress proteins in CNS inflammation. J Pathol. 2008;214(2):267–75.
101. Keck S, Nitsch R, Grune T, Ullrich O. Proteasome inhibition by paired helical filament-tau in brains of patients with Alzheimer's disease. J Neurochem. 2003;85(1):115–22.
102. Zabel C, Nguyen HP, Hin SC, Hartl D, Mao L, Klose J. Proteasome and oxidative phoshorylation changes may explain why aging is a risk factor for neurodegenerative disorders. J Proteomics. 2010;73(11):2230–8.
103. McClellan AJ, Frydman J. Molecular chaperones and the art of recognizing a lost cause. Nat Cell Biol 2001;3(2):E51-53.
104 Figueiredo-Pereira ME, Rockwell P, Schmidt-Glenewinkel T, Serrano P. Neuroinflammation and J2 prostaglandins: linking impairment of the ubiquitin-proteasome pathway and mitochondria to neurodegeneration. Front Mol Neurosci 2015;7:104.
105. Perry G, Friedman R, Shaw G, Chau V. Ubiquitin is detected in neurofibrillary tangles and senile plaque neurites of Alzheimer disease brains. Proc Natl Acad Sci. 1987;84(9):3033–6.
106. Janke C, Kneussel M. Tubulin post-translational modifications: encoding functions on the neuronal microtubule cytoskeleton. Trends Neurosci. 2010;33(8):362–72.
107. Guzhova I, Kislyakova K, Moskaliova O, Fridlanskaya I, Tytell M, Cheetham M, Margulis B. In vitro studies show that Hsp70 can be released by glia and that exogenous Hsp70 can enhance neuronal stress tolerance. Brain Res. 2001;914(1–2):66–73.
108. Lancaster GI, Febbraio MA. Exosome-dependent trafficking of HSP70: a novel secretory pathway for cellular stress proteins. J Biol Chem. 2005;280(24):23349–55.
109. Fisher AB. Peroxiredoxin 6: a bifunctional enzyme with glutathione peroxidase and phospholipase A(2) activities. Antioxid Redox Signal. 2011;15(3):831–44.
110. Sorokina EM, Feinstein SI, Zhou S, Fisher AB. Intracellular targeting of peroxiredoxin 6 to lysosomal organelles requires MAPK activity and binding to 14-3-3ε. Am J Physiol Cell Physiol. 2011;300(6):1430–41.
111. D'Silva AM, Hyett JA, Coorssen JR. Proteomic analysis of first trimester maternal serum to identify candidate biomarkers potentially predictive of spontaneous preterm birth. J Proteomics. 2018;178:31–42.